Geomorphology 248 (2015) 77–92

Contents lists available at ScienceDirect

Geomorphology

journal homepage: www.elsevier.com/locate/geomorph

Database and spatial distribution of landslides triggered by the Lushan, China Mw 6.6 earthquake of 20 April 2013

Chong Xu [a,b,*], Xiwei Xu [a], J. Bruce H. Shyu [b]

[a] Key Laboratory of Active Tectonics and Volcano, Institute of Geology, China Earthquake Administration, Beijing 100029, China
[b] Department of Geosciences, National Taiwan University, Taipei, Taiwan

ARTICLE INFO

Article history:
Received 26 January 2015
Received in revised form 30 June 2015
Accepted 1 July 2015
Available online 7 July 2015

Keywords:
2013 Lushan earthquake
Landslide inventory
Landslide database
Spatial analysis
Satellite images

ABSTRACT

On 20 April 2013, an earthquake with Mw 6.6 (Ms 7.0) hit Lushan County, Sichuan Province of China (30.3°N, 103°E), only 85 km southwest of the 2008 Wenchuan Mw 7.9 event. The Lushan shock triggered a large number of landslides with various types, including highly disrupted shallow slides and rock falls, deep-seated landslides and large-scale rock avalanches. Post-earthquake high resolution aerial photographs and satellite images, as well as a series of pre-earthquake high resolution satellite images were collected to construct a detailed, accurate, objective, and complete coseismic landslide database/inventory, which was validated by field investigation in selected areas. Based on the aerial photographs (0.2 or 0.6 m resolution) that partly cover the affected area and pre-earthquake satellite images, 14,580 coseismic landslides were recognized and mapped. In those areas without post-earthquake aerial photographs coverage, we mapped 7,948 more coseismic landslides based on post-earthquake satellite images (Rapideye images with 5 m resolution and ZY-3 images including panchromatic images with 2.1 m resolution and multi-spectral images with 5.8 m resolution) and pre-earthquake satellite images. The 22,528 coseismic landslides, with a horizontal projection area of 18.88 km^2 and an estimated total volume of 41.56×10^6 m^3, were distributed in a nearly elliptic area of about 5,400 km^2. Correlations between coseismic landslide abundances and topographic, geologic, and seismic factors were analyzed on 15,546 landslides of area ≥100 m^2. Scatter plots between regional slope angle and landslide abundances in generalized homogeneous lithology combinations show no obvious relationship is present between them, which challenges the conclusions of previous studies. Combining the Lushan earthquake-triggered landslides with other events on reverse and/or thrust faults such as the 1999 Chi-Chi and 2008 Wenchuan shocks, we found that coseismic landslides tend to occur in areas enveloped by two or more imbricated reverse and/or thrust faults, rather than only along the seismogenic fault. The Lushan event shows a higher ability of triggering landslides compared with other earthquakes of similar magnitudes, which is likely due to the steep and rugged topography and fractured and densely jointed lithology resulted from long-term tectonic activity. The blind reverse seismogenic fault is likely also another significant factor. Based on detailed coseismic landslide inventory maps and databases of several recent major earthquakes such as the 2008 Wenchuan, 2010 Haiti, 2010 Yushu, and 2013 Lushan temblors, we suggest that the empirical correlations between earthquake magnitude and coseismic landslides need to be updated.

1. Introduction

Through the history of earthquake-triggered landslides study, researchers have been working hard to understand the fundamentals of earthquake-triggered landslide occurrences, mechanisms, and distributions. Researchers have endeavored to discover the spatial distribution patterns of these landslides and their controlling factors. Constructing an objective and complete coseismic landslide inventory or database is important. The 1811 New Madrid, Missouri, earthquake is probably the first event with such an inventory (Keefer, 1984, 2002; Jibson and Keefer, 1989). Researchers successively constructed coseismic landslide inventories or databases of various types, including maps from retrospective studies, paper-based maps, and digital vector maps (Keefer, 2002), and alias database. Their quality and quantity are not always satisfactory due to limitations of remote sensing and GIS technologies in the past, randomness of earthquake occurrence, and the lack of uniform criteria. In recent years, the criteria of landslide inventorying have been proposed and gradually improved (Liao and Lee, 2000; Keefer, 2002; Harp et al., 2011; Guzzetti et al., 2012; Xu, 2014a). They can guide researchers to produce detailed and complete landslide inventories and to carry out subsequent objective scientific studies concerning landslide distribution (Gorum

* Corresponding author at: Key Laboratory of Active Tectonics and Volcano, Institute of Geology, China Earthquake Administration, Beijing 100029, China.
E-mail addresses: xc11111111@126.com, xuchong@ies.ac.cn (C. Xu), xiweixu@vip.sina.com (X. Xu), jbhs@ntu.edu.tw (J.B.H. Shyu).

http://dx.doi.org/10.1016/j.geomorph.2015.07.002

et al., 2011; Meunier et al., 2013; Tatard and Grasso, 2013; Xu, 2014b; Xu and Xu, 2014a), susceptibility, hazard, and risk assessments (Lee et al., 2008; C. Xu et al., 2013a, b), landform evolution (Parker et al., 2011; G. Li et al., 2014; Xu et al., 2014a; Y. Li et al., 2014), relation with debris flows (Tang et al., 2012; Zhou and Tang, 2014), and post-earthquake vegetation recovery (Khattak et al., 2010; Wang et al., 2014). It should be noted that in previous publications "landslide inventory" is a more common expression than "landslide database". This is because only landslide distribution or an inventory map was available for an old event when advanced GIS technology was absent, for example, the 1970 Peru (Plafker et al., 1971), the 1976 Friuli, Italy (Govi, 1977), the 1976 Guatemala (Harp et al., 1981), and the May 1980, Mammoth Lakes, California (Harp et al., 1984) earthquakes. Later, the development of GIS resulted in quite a few landslide databases for individual events, such as the 1994 Northridge, California (Harp and Jibson, 1995), the 1999 Chi-chi, Taiwan (Liao and Lee, 2000), the 2008 Wenchuan, China (C. Xu et al., 2009a; Dai et al., 2011a; Gorum et al., 2011; Xu et al., 2014b), the 2010 Yushu, China (Xu and Xu, 2014a), the 2010 Haiti (Gorum et al., 2013; Xu et al., 2014c), and the 2013 Minxian, China (Xu et al., 2014d) earthquakes. The database related to the Northridge earthquake is probably the first GIS-based digital landslide database, in which an individual landslide corresponds to one record. The record can also include attributes such as landslide area, volume, length, width, height, slope angle, aspect, and lithology. However, the landslide database is still more popular than landslide inventory due to personal habits of researchers. Nevertheless, in our opinion, "*landslide database*" is more appropriate than "*landslide inventory*" for a set of GIS-based landslide records since the 1994 Northridge, California event.

Here we briefly describe the historical and state of art of earthquake-triggered landslide inventory or database. Keefer (1984) collected 40 individual earthquake events that occurred before 1980 and correlated earthquake magnitudes with the landslide-distribution area, maximum distance from the epicenter, and distance from fault-rupture zones for those events. He also drew corresponding upper margins to represent the maximum values of indexes of earthquake-triggered landslides for the events of certain magnitude. Subsequently, Rodriguez et al. (1999) slightly adjusted the margins based on 36 individual shocks of 1980 to 1997. Although more events were added to verify the reliabilities of these margins (Liao and Lee, 2000; Bozzano et al., 2004; Jibson et al., 2004a; Khazai and Sitar, 2004; Agnesi et al., 2005; Keefer et al., 2006; Dai et al., 2011a; Xu and Xu, 2014a; Xu et al., 2014b), the binary correlations between earthquake magnitudes and earthquake-triggered landslides remain rough, and cannot clearly reveal the spatial distribution patterns of earthquake-triggered landslides and how the controlling factors work. More and more researchers realized that a detailed and complete inventory or database of earthquake-triggered landslides is very useful (Keefer, 2002; Harp et al., 2011; Xu, 2014a).

In recent years, a series of detailed and complete earthquake-triggered landslide inventories or databases were constructed and correlations between earthquake-triggered landslides and topographic, geologic, and seismic factors were analyzed (Xu, 2014a; Xu et al., 2014b; and references therein). The inventory of landslides triggered by the 1994 Northridge, USA, Mw 6.7 earthquake is considered to be the first published detailed digital coseismic landslide inventory (Harp and Jibson, 1995; Keefer, 2002). The inventory was compiled based on visual interpretation of high-resolution aerial photographs. The resultant database registered about 11,000 coseismic landslides, covering about 23.8 km^2 and distributed in an area about 11,000 km^2. The 1999 Chi-Chi, Taiwan Mw 7.6 earthquake also triggered tens of thousands of landslides. Liao and Lee (2000) delineated 9,272 coseismic landslides in an area of 11,000 km^2 based mainly on visual interpretations of SPOT 4 satellite images. The landslides covered an area about 127.8 km^2. Later, a more detailed inventory was produced by visual interpretation of high-resolution aerial photographs (Wang et al., 2002). Many small-scaled landslides that cannot be identified on SPOT 4 images were detected and mapped. It shows the earthquake triggered at least 26,000 landslides in a total area about 170 km^2 (Wang et al., 2002). In addition, Lin et al. (2009) also presented a database for the earthquake-triggered landslides and the total area is only about 86 km^2. Therefore, it is likely that there are significant omission (false negative) errors. The landslides triggered by the 2008 Wenchuan, China earthquake received unprecedented attention. The coseismic landslides directly resulted in about 20,000 deaths (Yin et al., 2009). Among the landslides, there are many large-scaled landslides (Chigira et al., 2010; Dai et al., 2011b; Huang et al., 2012a, b) resulted in serious disasters, and even destroyed half of a county (Yin et al., 2009, 2015). Quite a few landslide databases related to the earthquake were produced (C. Xu et al., 2009a,b; Huang and Li, 2009; Qi et al., 2010; Xu et al., 2010, 2014b; Gorum et al., 2011; Parker et al., 2011; W.L. Li et al., 2013a; G. Li et al., 2014), including point- and polygon-based databases using visual interpretation or automatic extraction. The most detailed one registers 197,481 individual coseismic landslides, covering an area about 1,160 km^2, being distributed in 110,000 km^2 (Xu et al., 2014b). Most of the landslides (196,007 pieces) are distributed in an area about 44,000 km^2. In addition, an inventory of 828 coseismic landslide dams was also produced (Fan et al., 2012a,b). The most complete and detailed database (Xu et al., 2014b) has the largest number of landslides related to an individual great earthquake ever reported so far, and also include the database of the coseismic landslide dams. In addition, several earlier versions of the database have also been released (C. Xu et al., 2009a,b; Dai et al., 2011a). The detailed landslide database or the earlier versions have been widely used in subsequent studies: spatial analyses of coseismic landslides (C. Xu et al., 2009a,b; Dai et al., 2011a; Xu and Xu, 2012; Yuan et al., 2013; Xu et al., 2014b); susceptibility and hazard assessments based on bivariate statistics including weight of evidence (Xu et al., 2012a) and weight index (C. Xu et al., 2013a), logistic regression (C. Xu et al., 2013b), artificial neural network (Xu et al., 2012b), support vector machines (Xu et al., 2012c), and Newmark's method (X.L. Chen et al., 2014a); seismic intensity inversions (C. Xu et al., 2013c); and landscape changes of an earthquake affected area (Xu and Xu, 2013; Xu et al., 2014a). After the 2010 Port-au-Prince, Haiti, Mw 7.0 earthquake, plenty of high-resolution satellite images were accessible and available on the Google Earth platform. Several detailed coseismic landslide databases were constructed and spatial distribution analyses were performed (Gorum et al., 2013; Xu et al., 2014c). For the 2010 Yushu, China, Mw 6.9 earthquake, 2,036 coseismic landslides were delineated based on visual interpretation of very high resolution (0.2 or 0.4 m) aerial photographs and high resolution (2.5 m) satellite images, as well as selected field checking (C. Xu et al., 2013d; Xu and Xu, 2014a). This inventory is unprecedentedly detailed and complete for earthquakes generated by strike-slip faults. Other events with coseismic landslide databases include the 2005 Kashmir Mw 7.6 (Sato et al., 2007; Kamp et al., 2008; Owen et al., 2008), the 2004 Mid-Niigata, Japan, Mw 6.6 (Sato et al., 2005), the 2003 Lefkada, Greece, Mw 6.3 (Papathanassiou et al., 2013), the 2002 Alaska, USA, Mw 7.9 (Jibson et al., 2004b; Gorum et al., 2014), and the 2013 Minxian, China, Mw 5.9 (Xu et al., 2014d) earthquakes. These databases can help assess and mitigate landslide hazards in earthquake affected areas.

On April 20, 2013, an earthquake of Mw 6.6 (after the USGS) or Ms 7.0 (after the China Earthquake Network Center) struck Lushan County, Sichuan Province of China. As of 14:30 (Beijing Time) of April 24, 2013, this earthquake caused 196 deaths, 21 missing, and 11,470 injuries. As of 14:00 April 23, 2013 of Beijing time, a total of 3,509 aftershocks were recorded, the largest one is Ms 5.4. Similar to the main shock, almost all the aftershocks are of reverse- or thrust-faulting as shown by focal mechanism solutions (X.W. Xu et al., 2013a; J.S. Lei et al., 2014). This event not only resulted in serious casualties and property losses, but also triggered a larger number of landslides, which are of various types, including shallow highly disrupted rock falls and slides, and deep-seated landslides and large-scale rock avalanches (C. Xu et al., 2013e; Xu et al., 2015). A series of coseismic databases or inventory maps were produced (Table 1). Most of the published databases or inventory maps are emergent products that were finished in a short

Table 1
List of previous incomplete inventories of landslides triggered by the Lushan earthquake.

Type	*LN*	*LA* (km^2)	*LDA* (km^2)	Density (km^{-2})	References
Point	1,469		10,000	0.15	Wang (2015)
Point	421		320	1.32	Feng et al. (2013)
Polygon	703	1.2	122.11	5.76	Chang et al. (2013)
Polygon	1,379	5.85	6,651	0.2	Su et al. (2013)
Point	1,129		2200	0.51	X.L. Chen et al. (2014b)
Point	2231		1300	1.72	Zhou et al. (2014)
Point	1,460				Cui et al. (2014)
Point	1337				X. Z. Li et al. (2014)
Polygon	381	0.81	59.04	6.45	Zhang et al. (2013)
Point	2,037				W.L. Li et al. (2013b)
Point	688		200	3.44	Xu and Xiao (2013)
Point	3,883		2000	1.9	C. Xu et al. (2013e)
Point	15,640		2000	7.8	Xu(2013a)

Note: *LN*: landslide number; *LA*: landslide (areal) area, *LDA*: landslide distribution area.

time, which are helpful for quickly assessing the hazards caused by the landslides. However, none of them is detailed or complete. The presences of significant omission (false negative) errors are apparent. Based on an emergent coseismic landslide database (C. Xu et al., 2013e), we produced a more detailed one using available post-earthquake aerial photographs (Xu et al., 2015). The original inventory map registered 3,880 landslides (C. Xu et al., 2013e) and 11,760 more landslides were recognized by more careful visual interpretation of the same aerial photographs (Xu et al., 2015). However, this landslide inventory map remains incomplete because the post-earthquake aerial photographs do not cover the entire affected area.

The purpose of this paper is to construct a more detailed, objective and complete landslide database related to the 2013 Lushan event based on the previous incomplete database and supplementary remote sensing data, including post-earthquake high-resolution Rapideye and ZY-3 satellite images. The resulted coseismic landslide inventory map was then validated by field inspection in selected areas. This study also focuses on the correlation between the distribution of coseismic landslides and topographic, geologic, and seismic factors. In addition, several issues are discussed, including correlations between topography and coseismic landslide abundance in generalized homogeneous lithology combinations, the distribution pattern of coseismic landslides related to earthquakes occurred on imbricated reverse and/or thrust faults, and the higher capability of the Lushan earthquake to trigger landslides.

2. Geologic setting

The collision of the Indian and Eurasian plates resulted in the uplift of the Tibetan Plateau and eastward motion of a series of blocks in this highland (Chen et al., 2000; Tapponnier et al., 2001; Wang et al., 2001; Gan et al., 2007). Obstructed by the rigid Sichuan Basin, the Longmenshan thrust zone formed along the boundary between the Tibetan Plateau and Sichuan Basin (Xu et al., 2008), at which the accumulated strain is released during frequent earthquakes (X.W. Xu et al., 2009; Zhang et al., 2010). Both the 2008 Wenchuan and the 2013 Lushan temblors occurred on this northeast-trending fault zone. The epicenter of the Lushan event is located only 85 km southwest of the 2008 Wenchuan shock (Fig. 1).

The Longmenshan thrust zone is composed of three main thrust fault systems, which are the Maoxian-Wenchuan fault (also called back-range fault), the Yingxiu-Beichuan fault (also called central fault), and the Guanxian-Jiangyou fault (also called front-range fault) from northwest to southeast. In addition, a fault buried by the piedmont, southeast of the three faults, showing features of forward-propagating deformation, is also considered as a secondary fault of the Longmenshan thrust zone (Chen et al., 1994; Deng et al., 1994; Royden et al., 1997; Clark and Royden, 2000). Furthermore, the three fault systems aforementioned contain sub-faults (Fig. 1). For example, the Qingchuan-Pingwu fault

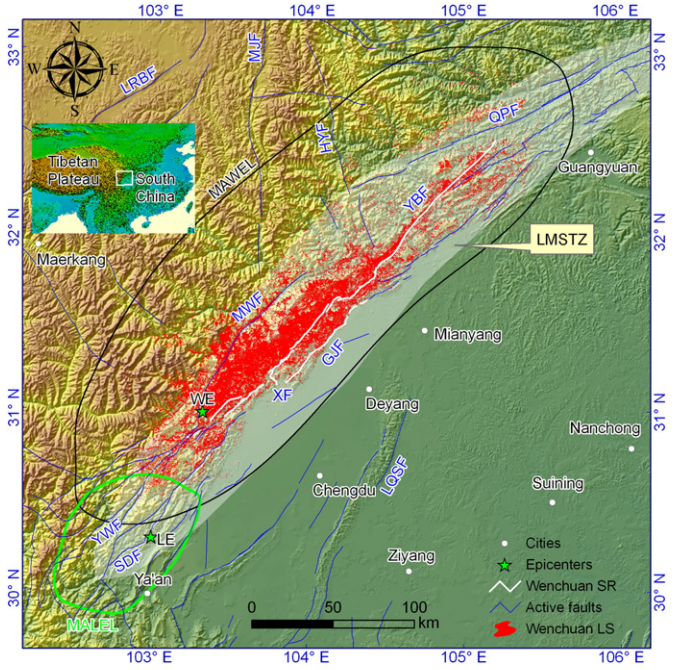

Fig. 1. Tectonic setting of the Longmenshan thrust belt and the affected areas of the Wenchuan and Lushan earthquakes. LE: Lushan earthquake epicenter; WE: Wenchuan earthquake epicenter; LMSTZ: the Longmenshan thrust zone; YBF: the Yingxiu-Beichuan fault; QPF: the Qingchuan-Pingwu fault; MWF: the Maoxian-Wenchuan fault; HYF: the Huya fault; LRBF: the Longriba fault; MJF: the Minjiang fault; XF: the Xiaoyudong fault; YWF: the Yanjing-Wulong fault; LQSF: the Longquanshan fault. MAWEL: the main area affected by the Wenchuan earthquake-triggered landslides; MALEL: the main area affected by the Lushan earthquake-triggered landslides. This area is shown as the white rectangle in the sub panel in the upper left corner.

and the Maoxian-Wenchuan fault belong to the back-range fault system. The Yingxiu-Beichuan fault and the Yanjing-Wulong fault are part of the central fault system. The Guanxian-Jiangyou fault and the Shuangshi-Dachuan fault are members of the front-range fault system.

The 2013 Lushan earthquake occurred on the southwestern segment of the Longmenshan thrust zone, whereas the Wenchuan event occurred on the central part of the belt. Although the epicenters of them are only about 85 km apart, the two events are not considered to be generated by the same fault. The Wenchuan earthquake was spawned by the Yingxiu-Beichuan fault, with three surface ruptures on three faults, i.e. the Yingxiu-Beichuan, Guanxian-Jiangyou, and Xiaoyudong faults (X.W. Xu et al., 2009; Tan et al., 2012). The epicenter of the Lushan event is, on the other hand, located near the Shuangshi-Dachuan fault. Since there is a nearly 40-km-long rupture gap between the Lushan and the Wenchuan earthquakes (Chen et al., 2013), most researchers do not consider the Lushan event to be an aftershock of the Wenchuan shock, but an independent one (X.W. Xu et al., 2013b; Jia et al., 2014; L.C. Chen et al., 2014). On the other hand, the epicenter of the Lushan quake is located at the Coulomb stress increasing zones after the 2008 Wenchuan event (Parsons et al., 2008; Toda et al., 2008; Shan et al., 2013). Therefore, the latter might be an important trigger for the former. In other words, the 2008 Wenchuan great shock may have speeded up the occurrence of the 2013 Lushan earthquake.

In the Lushan temblor affected area, there are three major northeast-striking faults: the Yanjing-Wulong, the Shuanshi-Dachuan, and the Western Shangli faults from northwest to southeast (Fig. 2). It was originally proposed that the Shuangshi-Dachuan fault was the seismogenic fault of the Lushan event based on preferred nodal planes of focal mechanism solutions and regional tectonic setting. However, after subsequent field investigations, more detailed analyses of seismic waves, focal mechanism solutions and spatial distribution of aftershocks, it is suggested that the seismogenic fault of the Lushan quake is a blind reverse fault southeast of the Shuangshi-Dachuan fault (C.Y. Li et al.,

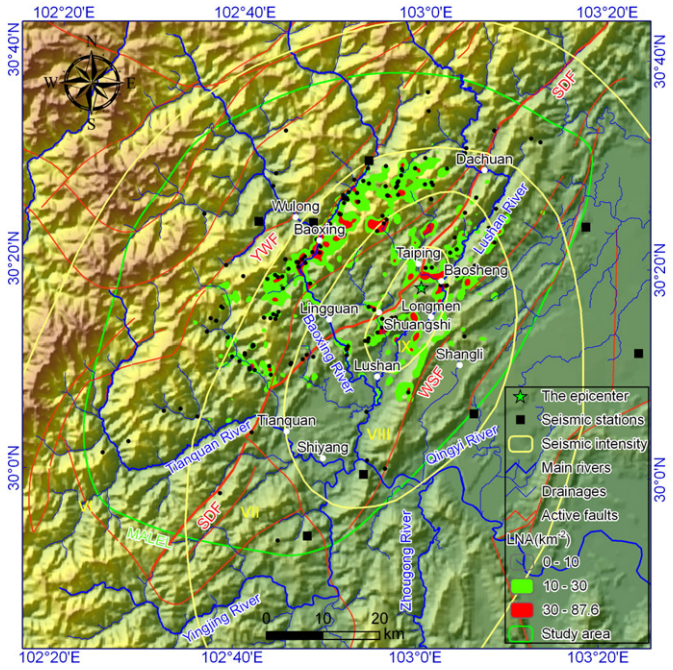

Fig. 2. Regional tectonic setting of the Lushan earthquake affected area. YWF, the Yanjing-Wulong fault; SDF, the Shuangshi-Dachuan fault; WSF, the Western Shangli fault. The solid black dots are 162 coseismic landslides of area >10,000 m^2. Areas of the *LNA* value ranges 30–87.6 km^{-2}, 10–30 km^{-2}, and <10 km^{-2} are 55.47 km^2, 385.36 km^2, and 4955.17 km^2, respectively.

2013; X.W. Xu et al., 2013a). Earthquakes occurred on blind reverse faults that did not broken the ground surface are quite common, such as the 2010 Haiti Mw 7.0 (Calais et al., 2010; Hayes et al., 2010), the 1994 Northridge, USA, Mw 6.7 (Hauksson et al., 1995), the 1989 Loma Prieta, USA, Mw 6.9 (Prentice and Schwartz, 1991; Árnadóttir and Segall, 1994), and the 1983 Coalinga, California, USA, Mw 6.2 (Stein and King, 1984) earthquakes. Although continuous ground surface rupture associated with the Lushan event was not seen, brittle compressive ruptures in cement-covered pavements have been found along a line from Shuangshi to Taiping and Dachuan, which are generally coincident with the Shuangshi-Dachuan fault (Han et al., 2013; X.W. Xu et al., 2013a). Similar compressive phenomena can also be observed along the line from Lushan to Longmen and Baosheng, and thus a blind reverse fault (called Lushan-Longmen blind fault) is proposed to exist in the area (C.Y. Li et al., 2013; Han et al., 2013). However, some of the phenomena likely resulted from shaking rather than actual fault rupturing, and a seismic investigation showed no evidence for the proposed Lushan-Longmen blind fault at least in the upper 800 m below the ground surface (S.X. Lei et al., 2014).

In the Lushan earthquake affected area, two historical earthquakes of M ≥ 6.0 with coseismic landslides are documented in history. One is the M6 shock in September 1327 (30.1°N, 102.7°E) that created a landslide dam in a river, about 150 m long, 40 m wide, and 10 m high. The dammed river overtopped after 10 hours after it was blocked (Disaster Prevention Department of National Seismological Bureau, 1995; Disaster Prevention Department of China Earthquake Administration, 1999). The other is the Ms 6.2 event on 24 February 1970 (30.65°N, 103.28°E).

On the eastern margin of the Tibetan plateau, the Longmenshan Mountain rises 6000 m above the Sichuan basin, with a greater topographic relief than anywhere else on the plateau (Burchfiel et al., 2008; Royden et al., 2008). The Lushan earthquake affected area is located at this high topographic relief area between the Tibetan Plateau and the Sichuan Basin. The major slope angles of the affected area range from 20° to 35°. From southeast to northwest, the terrain changes from plains and low hills to high mountains in the study area. The big topographic relief and steep hillslopes resulted from rapid crustal uplift and erosion in this area. The average erosion rate is 0.63–1.17 mm yr^{-1} in the affected area since 3–5 Ma (Arne et al., 1997; Richardson et al., 2008; Li et al., 2012; Cook et al., 2013; Tan et al., 2013). Ya'an City in the study area registers one of the highest annual precipitation records in a city in China. The annual precipitation of the city in the Lushan earthquake affected area is about 1800 mm (China Meteorological Data Sharing Service System, http://cdc.cma.gov.cn). The affected area has a subtropical humid monsoonal climate with quite dense vegetation cover.

3. Data and methods

3.1. Remote sensing images

In this study, we utilize aerial photographs and satellite images to construct coseismic landslide databases. The pre-earthquake images used include SPOT-5 images (panchromatic images of 2.5 m and multi-spectral of 10 m resolutions) collected on 3 June 2009, SPOT-4 images (panchromatic in 6.25 m and multi-spectral in 12.5 m) on 9 April 2011, Pleiades images (panchromatic in 0.5 m and multi-spectral in 2 m) on 22 January 2013, ZY02C images (panchromatic in 2.36 m and multi-spectral in 10 m) on 8 March 2013, ZY-3 images (panchromatic in 2.1 m and multi-spectral in 5.8 m) on 17 November 2012 and 30 March 2013, Landsat-5 images (multi-spectral in 30 m) on 18 March 2010, and images from the Google Earth platform.

The post-earthquake images (Rapideye and ZY-3) include high-resolution true-color aerial photographs and optical satellite images (Fig. 3). The aerial photographs of 0.2 and 0.6 m resolutions were acquired by the ADS80 digital aerial apparatus on unmanned aerial vehicles that began flying two and a half hours after the main shock to 22 April 2013. The Rapideye multi-spectral images (5 m resolution) were taken on 26 May 2013 and the ZY-3 panchromatic (2.1 m resolution) and multi-spectral (5.8 m resolution) images taken on 13

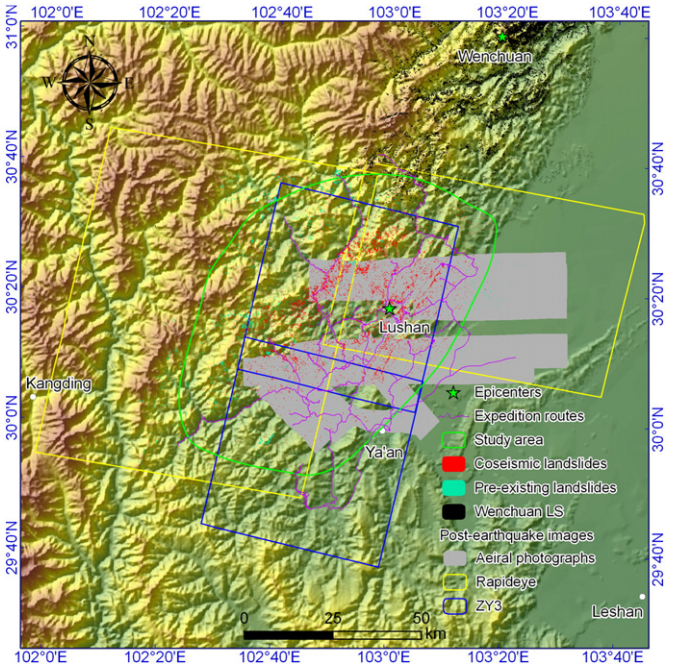

Fig. 3. Post-earthquake aerial photograph and satellite image coverages and landslides in the Lushan earthquake affected area. "Coseismic landslides" means landslides triggered by the 2013 Lushan earthquake. "Pre-existing landslides": landslides occurred before the Lushan earthquake excluding the Wenchuan earthquake-triggered landslides in the affected area. "Wenchuan LS": landslides triggered by the 2008 Wenchuan earthquake. One-way accumulated expedition routes excluding repeated survey routes during the field investigations exceed 1,000 km in length.

May 2013 (Fig. 3). The aerial photographs were ortho-rectified and georeferenced, and can be directly used to delineate coseismic landslides. Before landslide interpretation, the Rapideye and ZY-3 images were processed with some methods, including system calibration, orthorectification, geometric correction, data fusion, and true-color composite. All these procedures were performed on the ENVI platform.

3.2. Topographic, geologic, and seismic data

Available digital elevation models (DEMs) of the study area includes the SRTM DEM of 90 m and the ASTER GDEM of 30 m resolutions. Although the ASTER GDEM has higher resolution, it contains more noise and distortion. Therefore, we selected the SRTM DEM for this study. We resampled this DEM to a DEM of 10 m resolution using the bilinear method to improve statistical precision on areas of small-scale landslides. The resampling process would not add local topographic information, neither would it change the general topographic information of the original SRTM DEM data. The common topographic thematic maps of slope gradients and aspects were derived from the processed DEM of 10 m resolution. Slope position is a newly proposed factor that may affect coseismic landslide occurrence (Weiss, 2001; Jenness et al., 2013). The slope position thematic layer of the study area was extracted from a database of slope localities of China in Geospatial Data Cloud (www.gscloud.cn). Drainages of the affected area are extracted from the 10 m-resolution DEM and manually corrected based on high-resolution remote sensing images.

Lithology types and distances from faults were selected as the geological factors affecting earthquake-triggered landslides. The maps of lithology types and faults were derived from three parcels of the 1:200,000 geologic maps of the Tianquan (no. H-48-13, 30°–30°40′N, 102°–103°E), Qionglai (no. H-48-14, 30°–30°40′N, 103°–104°E), and Ya'an (no. H-48-19, 29°20′–30°N, 102°–103°E) areas of Sichuan Province, China. The underlying lithology of the study area was classified into 12 combinations (Table 2), from new to old, including (1) Quaternary (Q_4al, Q_3al, Q_3pl, Q_2fgl, Q_1fgl): Holocene river bed, modern alluvium, alluvium, sandy clay, and gravel; (2) Neogene and Paleogene (N_2Qpd, E_3l, $E_{1\text{-}2}mn$): coarse conglomerate, siltstone, and shale; (3) Cretaceous (K_2g, K_1g^2, K_1g^1, K_2j, K_1t): siltstone, silty mudstone, and feldspar sandstone intercalated with shale; (4) Jurassic (J_3p, J_2sn, J_2s, $J_{1\text{-}2}zl$): feldspar sandstone, fine sandstone, interbedded layer of siltstone and mudstone layers; (5) Triassic (T_3xj, T_3xj^2, T_3xj^1, T_2l, T_1j, T_1f): sandstone, dolostone, limestone, and dolomitic limestone; (6) Permian and Carboniferous (P_3w, P_2, P_2em, P_2c, P_2s, P_2x, P_2l, P_1y, P_1, P_1l, $P_1q + m$, C_{2+3}, C_1): quartz sandstone, siltstone, limestone, and shale; (7) Devonian (D), (D_3, D_3s, $D_{2\text{-}3}$, D_2, D_2y, D_2g, D_1p, D_1g, D_1, D_1^2, D_1^1): limestone, dolostone, quartz and sandstone; (8) Silurian (S), (S, S_3, $S_{2\text{-}3}$, S_2, S_2l, S_1, S_1l): sandy shale, dolomitic limestone, and mudstone; (9) Ordovician (O), (O_3, $O_{2\text{-}3}$, O_2, O_2b, O_1, O_1^3, O_1^2, O_1^1, $O_1h + q$): carbonaceous shale, siltstone and silty shale, and limestone; (10) Sinian (Sn), (Z_2, Z_2d, Z_1s, Z_1a): dolostone, phyllite, and volcanic breccia; (11) Pre-Sinian (Pre-Sn), (Pty, Pts, Pths^{2+3}, Pths^{3-2}, Pths^{3-1}, Pths^{2-2}, Pths^{2-1}, Pths^1, Pth, Ptf): amphibolite metamorphic basalt, chert; and (12) Intrusive rocks (I-rocks): granite, diorite, granodiorite, and gabbro.

Seismic data used in this study include the location of the epicenter, regional peak ground acceleration (*PGA*), seismic intensity, and the parameters of the seismogenic fault of the Lushan earthquake. The epicenter of the Lushan earthquake is located at 30.3°N, 103°E according to the China Earthquake Network Center (CENC, www.cenc.ac.cn). Although there were a series of real-time vibration data from seismic stations recorded during the main shock (CSMNC, www.csmnc.net), only a few of which are near the epicenter (Fig. 2). Therefore, it is difficult to get *PGA* values based only on data interpolation from seismic stations in operation. The US Geological Survey (USGS, www.usgs.gov) released a series (4 versions) of *PGA* maps related to the Lushan earthquake (US Geological Survey, 2013). The Version 1 was only based on a simulation-based method without considering the geometry of the seismogenic fault, whereas Version 4 with a moderate objectivity was obtained from a combination of regional tectonic settings, records from a few seismic stations, and numerical simulations. The *PGA* map of version 4 with a moderate uncertainty is more objective and accurate than the previous versions. Therefore, we used the Version 4 *PGA* map to correlate coseismic landslides with the ground shaking. The "Seismic Intensity Map of the 2013 Lushan Earthquake" was released by the China Earthquake Administration several days after the earthquake, mainly based on field investigations. Since the Lushan event was presumably caused by breaking of a blind reverse fault without surface ruptures, we used the preferred nodal plane from several released focal mechanism solutions of the main shock to represent the seismogenic fault of the earthquake.

3.3. Methods

3.3.1. Landslides detection

The methods for landslide detection include field investigations, visual interpretation of paper-based stereo-pair aerial photographs with the aid of stereo microscopes, identification of landslides from a high resolution DEM (e.g., LiDAR), visual interpretation of high resolution satellite ortho-images, deformation analysis from multi-temporal radar images based on InSAR technology, and automatic identification of landslides from optical remote sensing images (e.g. Keefer, 2002; Harp et al., 2011; Guzzetti et al., 2012; Xu, 2014a). For earthquake-triggered landslides, especially shortly after the earthquake, areas affected by coseismic landslides would always show an obviously different appearance from the surrounding areas on optical remote sensing

Table 2
Generalized lithology combinations in the study area.

Types	*M-SloAng* (°)	*P-SloAng* (°)	*PGA-V*	*EPI-V*	*LAA* (‰)	*PGA-N LAA* (‰)	*EPI-N LAA* (‰)
Quaternary (Q)	8.8	1	7.5	26.7	2.59	0.35	0.1
Neogene (N) and Paleogene (P)	15.6	10.9	6.2	24.5	3.51	0.57	0.14
Cretaceous (K)	21	17.5	7.5	22.5	3.26	0.43	0.14
Jurassic(J)	19	17.4	8.9	26	1.76	0.2	0.07
Triassic (T)	22.2	22.7	5.5	24.4	4.44	0.81	0.18
Permian (P) and Carboniferous (C)	27	25.6	7.3	28.8	4.62	0.63	0.16
Devonian (D)	29.6	31	9.5	38.5	1.72	0.18	0.04
Silurian (S)	29.1	29.4	9.7	40.1	1.28	0.13	0.03
Ordovician (O)	30.4	34	11	44.2	1.01	0.09	0.02
Sinian (Sn)	30.5	32.8	10.3	46.1	3.45	0.34	0.07
Pre-Sinian (Pre-Sn)	31.2	33.9	9.5	32	0.94	0.1	0.03
Intrusive rocks (I-rocks)	31	34.6	9.2	38.7	7.78	0.85	0.2

Note: *M-SloAng*: mean values of slope angle in homogeneous lithology types; *P-SloAng*: peak values of slope angle in homogeneous lithology types; *PGA-V*: *PGA* value proxies in homogeneous lithology types; *EPI-V*: proxy values of distance from the epicenter in homogeneous lithology types; *LAA* (‰): landslide area abundance. "*PGA-N LAA*": *LAA* values normalized by *PGA-V*, "*EPI-N LAA*": *LAA* values normalized by distance from the epicenter (*EPI-V*).

images. Coseismic landslides can be easily recognized and detected on images with high resolutions (~1–10 m or higher), which are almost comparable with results from field investigations. In addition, landslides triggered by large earthquakes are usually large in number with high density and broad distribution, thus it is not realistic to prepare a detailed coseismic landslide database based only on field investigations. Therefore, the most suitable method of this study is visual interpretation of high-resolution remote sensing images, which is then verified by field inspection in selected areas. With the aid of computer, GIS and remote sensing technologies, we used a method of syntheses of computer screen-based visual interpretation of high-resolution aerial photographs and satellite images on the GIS platform, which has been shown to be the most objective and best method for this issue (Liao and Lee, 2000; Dai et al., 2011a; Harp et al., 2011; Gorum et al., 2013; Xu, 2014a; Xu et al., 2014b, 2014c, 2014d).

The quality of a coseismic landslide inventory map or database depends upon three aspects, which are the accuracy of geographic location of landslides, the amount of omission (false negative) errors and quantity of commission (false positive) errors. In order to ensure the geographic location accuracy of the landslides, we collected a series of actual GPS routes and points from field investigations to correct the remote sensing images. The deviations between the GPS data and remote sensing images were lower than one grid of the Rapideye and ZY-3 images (~5 m). In order to limit omission errors, we collected aerial photographs and satellite images of high resolutions that cover the entire earthquake affected area. Although the aerial photographs of 0.2 and 0.6 m resolutions do not cover the entire earthquake affected area, we obtained supplementary Rapideye and ZY-3 satellite images with resolutions of 5 and 2.1 m. This ensured the landslides larger than 100 m^2 can clearly be shown on the images. In addition, we used a computer with screen height of about 300 mm, and zoomed in the image so that the actual length on the image in a computer screen was about 300 m. This is equivalent to working on images of a scale 1:1,000, and ensures that almost all landslides clearly displayed on the images can be recognized, and delineated. To limit commission errors, we checked every landslide on pre-earthquake images to distinguish pre-earthquake landslides from coseismic landslides by the methods mentioned by Xu (2014a). Since the post-earthquake aerial photographs were taken within three days after the main shock, and the satellite images were taken within about one month after the main shock, very few non-seismic landslides occurred after the main shock and appeared on the images. Although rainfalls did occur during those days, the number of the landslides triggered by these rainfalls or other factors after the main shock would be quite limited. Furthermore, since the post-earthquake images we used were taken shortly after the main shock, most of the coseismic landslides would preserve their original shapes, with very few new vegetation covers on landslide bodies that could affect the visual interpretation.

3.3.2. Field inspection

Although a large number of high-resolution remote sensing images were available, and the accuracy of inventory maps and databases based only on visual interpretation of pre- and post- earthquake images has already become satisfactory (Xu et al., 2014c), we still carried out filed investigations to validate the coseismic landslide inventory map. Two stages of filed investigations were performed, which are the emergent field reconnaissance from the day of the main shock to 1 May 2013 (C. Xu et al., 2013e) and the detailed filed investigation lasting 27 days from 25 May 2013 (Xu et al., 2015). In total, one-way accumulated expedition routes excluding repeated survey routes during the two stages of field investigations exceed 1,000 km in length (Fig. 3; Xu et al., 2015). The major access of the field area was by car, next by walking. We were able to observe all coseismic landslides mapped on remote sensing images that we selected in the field inspection. However, some very small-scale landslides (<50 m^2 in area), mostly as blocks rolling downhill, cannot be observed on the 5 m resolution Rapideye satellite images, but can usually be seen on the 0.2 and 0.6 m resolution aerial photographs. Therefore, in order to eliminate the uneven omission errors with those very small-scaled landslides in the subsequent spatial distribution analyses, all coseismic landslides of an area less than 100 m^2 were excluded in the subsequent analysis.

3.3.3. GIS spatial analysis of coseismic landslides

Landslide abundance (or landslide density) is a common index to measure patterns and characteristics of coseismic landslides. It generally includes three different indexes, which are the landslide number abundance (*LNA*), area abundance (*LAA*), and volume abundance (*LVA*). *LNA* is defined as the number of landslides per square kilometer, *LAA* is the percentage of the area affected by the landslides, and *LVA* is the average thickness of landslide materials in a given area, which is calculated by dividing the volume of coseismic landslides with the given area. *LNA* and *LAA* are commonly used in previous studies. In earlier studies, due to the lack of advanced remote sensing and GIS technologies, it was difficult to determine the boundary and area of coseismic landslides, thus usually only *LNA* was calculated (Jibson and Keefer, 1989; Keefer, 2000), with occasionally *LAA* reported (Tibaldi et al., 1995). Although *LNA* is easy to calculate, the scales of coseismic landslides cannot be reflected in this parameter. With the maturation of GIS and remote sensing technologies, more and more coseismic landslide inventory maps are polygon-based. Therefore, with a few exceptions (Sato et al., 2007; Qi et al., 2010; Gorum et al., 2011), most recent studies report *LAA* as the statistical index (Liao and Lee, 2000; Sepúlveda et al., 2010; Dai et al., 2011a; C. Xu et al., 2013d; Gorum et al., 2013, 2014; Basharat et al., 2014; Xu and Xu, 2014a; Xu et al., 2014b). Although making a polygon-based landslide inventory map is time-consuming, it is warranted because it is more accurate than point-based inventory maps for landslides susceptibility and hazard assessments (Xu et al., 2012c). Moreover, landslide "area to volume" power-law relations have been recently employed in many regions of the world (ten Brink et al., 2006; Guzzetti et al., 2009; Larsen et al., 2010; Parker et al., 2011), which make *LVA* in coseismic landslides distribution analyses available (Xu and Xu, 2013; Xu et al., 2014c). Therefore, we selected the three indexes to perform spatial distribution analyses of the landslides. It should be noted that landslide volume was calculated based on a simple scaling relationship to convert an individual landslide area into individual landslide volume:

$$V_i = \alpha \times A_i^{\gamma} \quad (1)$$

where V_i represents the volume of a landslide (i-th landslide) and A_i is the area occupied by the landslide. The two scaling parameters α and γ vary with different landslide types and cases. We assigned $\alpha = 0.146$ and $\gamma = 1.332$, which are derived from various types of landslides (Larsen et al., 2010) and have been used in previous studies (Parker et al., 2011; Xu et al., 2014c, 2014e).

4. Analysis and results

4.1. Database of landslides triggered by the Lushan earthquake

We delineated in total 27,259 landslides based on post-earthquake aerial photographs and satellite images (Rapideye and ZY-3) in the earthquake affected area (Fig. 3). Of these, 4,731 landslides were confirmed to be present before the earthquake based on pre-earthquake images and do not show any signs of enlargement or remobilization during the event. The remaining 22,528 landslides, either newly formed landslides or remobilized or enlarged of old landslides, are considered as coseismic landslides (Fig. 4). The 22,528 landslides, with 18.88 km^2 in total area and 41.56×10^6 m^3 in total volume, are distributed in an area about 5,400 km^2 (Fig. 4). Compared with the landslides triggered by the 2008 Wenchuan earthquake (Xu, 2013b; Xu et al., 2014b) which are 197,481 in number, about 1,160 km^2 in occupying area,

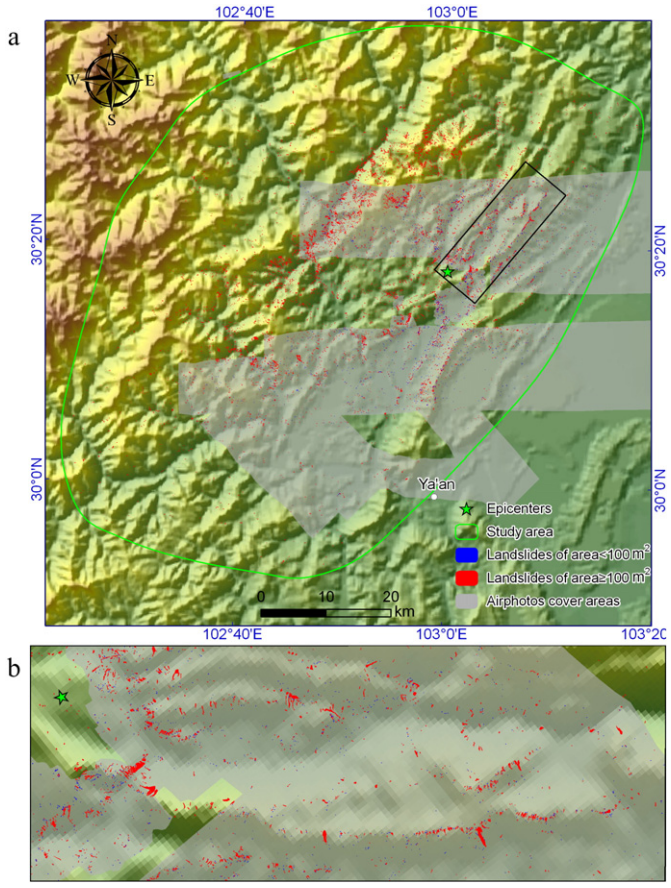

Fig. 4. a) Inventory map of landslides triggered by the Lushan earthquake. b) the enlarged area of the black rectangle on (a).

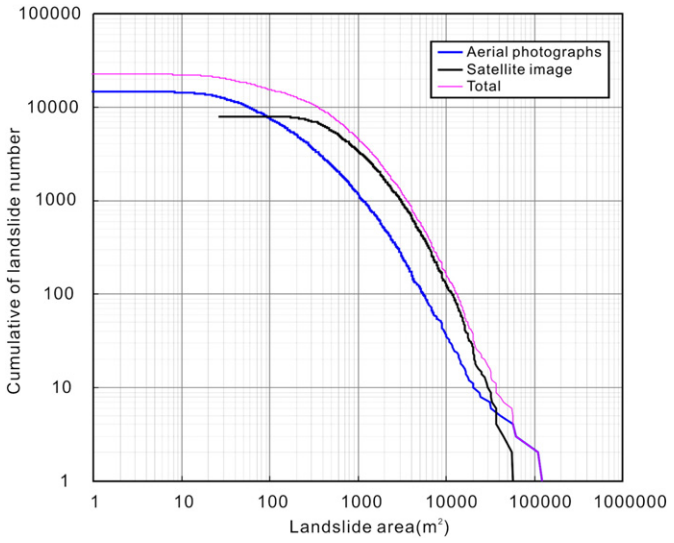

Fig. 5. Curves depicting correlations between cumulative landslide number and the landslide area of inventories obtained by different datasets.

about 6 km^3 in landslide volume, and about 110,000 km^2 in landslide distribution area, the landslides triggered by the Lushan earthquake equal to about 1/9 in number, 1/60 in occupying area, 1/150 in volume, and 1/20 in distribution area of those of the Wenchuan event, respectively.

Among the 22,528 coseismic landslides induced by the Lushan earthquake, 14,580 landslides were detected from the high resolution aerial photographs, while 7,948 landslides were recognized on Rapideye or ZY-3 satellite images. Of these, 162 landslides are of area ≥ 10,000 m^2, 4,378 landslides are between 1,000 and 10,000 m^2, 11,006 landslides are between 100 and 1,000 m^2, and the remaining 6,982 are <100 m^2. Most of the landslides are relatively shallow slides, typically 1–5 m in depth. Although large-scale deep-seated landslides and rock avalanches are less than small shallow disrupted landslides, the former contribute to the total volume of landslide material due to their large sizes. The largest landslide triggered by the Lushan earthquake is the Pingtou rock avalanche (or double rock avalanches) that occurred in the Tangjiagou gully, Damiao village, Baoxing county, lying on a ridge (30°10′43″N, 102°45′40″E). The rock avalanche, with a total volume about 1.5×10^6 m^3, originated from two connected parts, formed two movement paths and finally gathered together in the accumulated area (Xu et al., 2015).

Since almost all the 6,982 small landslides of area < 100 m^2 were detected on the aerial photographs with high resolution of 0.2 or 0.6 m, we exclude those small ones in the subsequent analysis. The 6,982 landslides only cover 0.33 km^2 and moved 0.185×10^6 m^3 materials. Although the remaining 15,546 large landslides (area ≥100 m^2, see the Supplementary material) only accounted for 69% of the total coseismic landslide number, they dominated the landslide area and volume, which are 18.55 km^2 and 41.375×10^6 m^3, or 98.25% and 99.55% of the total, respectively. Therefore, the subsequent spatial analyses with only the large landslides can reflect the predominant situation of the Lushan earthquake-triggered landslides.

The curves depicting the correlations between the cumulative landslide number and the landslide area related to three landslide inventories were prepared (Fig. 5). The first is the landslide database obtained from the aerial photographs (contains 14,580 landslides), the second is from Rapideye or ZY-3 images (contains 7,948 landslides), and the third is the final merged inventory of the first two inventories (contains 22,528 landslides). Although all three curves bend towards horizontal in small landslides areas, the curve related to the aerial photographs bends towards horizontal when the area is smaller than about 10–20 m^2, whereas the curve related to the satellite images bends so when the area is smaller than about 100–200 m^2. This difference may be attributed to the omission of small-scale landslides in the inventory based on satellite images. Such omission of landslides with area < 200 m^2 is perhaps due to coalescing small landslides mapped as one large landslide, or the difficulty to observe smaller landslides on the images with a resolution of about 5 m. Therefore, we selected 100 m^2 as the landslide area threshold, which means only landslides of area ≥ 100 m^2 are used in the following analyses.

4.2. Correlation of landslide density with controlling factors

To draw the curves of statistical correlations between controlling factors and the three indexes of landslide abundance on each panel, the units of *LNA*, *LAA*, and *LVA* are set to be km^2 or km^{-2}, ‰, and mm, respectively. The topographic controlling factors include elevation, slope angle, slope aspect, slope position, and distance from drainages. The geologic factors refer to lithology types and distance from faults. The seismic factors are *PGA*, seismic intensity, distance from the epicenter, distance from the probable seismogenic fault, and distance along the probable seismogenic fault.

4.2.1. Topographic factors

The correlations between the five topographic factors and three landslide abundance indexes are displayed in Fig. 6. The elevations of the study area range from 543 to 4,852 m, while almost of the whole area (4,977 km^2, 92.2% of the total) are lower than 3,000 m. All three curves in each graph show similar tendencies, which indicates that most landslides of different scales are roughly uniformly distributed in areas with different elevation intervals and all the three landslide abundance indexes can be used to carry out spatial distribution analysis. The elevation interval between 1,000 and 1,500 m has the largest landslide

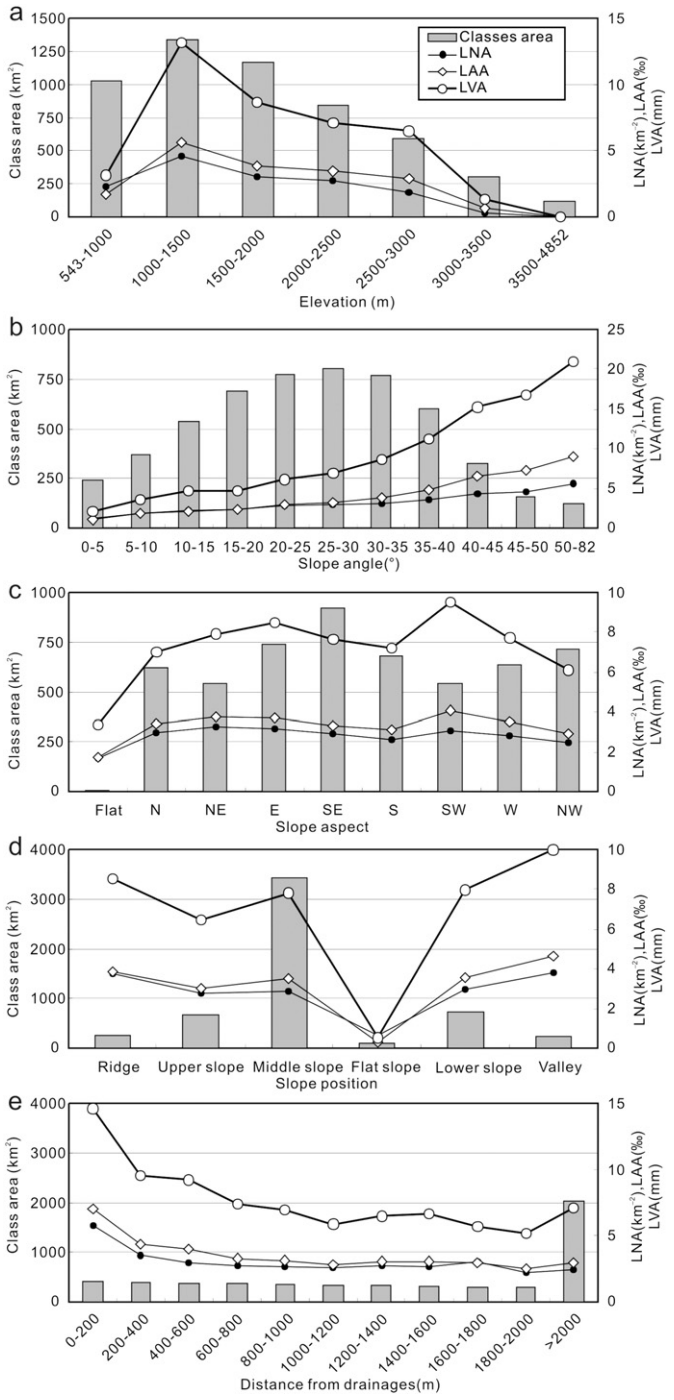

Fig. 6. Correlations of topographic factors with landslide abundance proxies. a) elevation; b) slope aspect; c) slope aspect; d) slope position; e) distance from drainages.

abundances, which are 4.59 km^{-2} in *LNA*, 5.61‰ in *LAA*, and 13.21 mm in *LVA* (Fig. 6a). The landslide abundance values gradually decrease at the elevations higher than 1,500 m.

The slope angle is an essential impact parameter to coseismic landslides occurrence. In general, the higher the slope angle, the higher the probability of earthquake-triggered landslides. The slope angle of the study area ranges from 0° to 82° which is divided into 11 classes with an interval of 5°. Slope angles of most of the study area (4,182 km^2, 77.5%) are between 10° and 40° (Fig. 6b). It seems that the three landslide abundance values increase with the slope angle, particularly for slope angles exceeding 30°. The maximum *LNA*, *LAA*, and *LVA* occurred at slope angles higher than 50°, and their values are 5.57 km^{-2}, 9.03‰, and 20.94 mm, respectively.

Different slope aspects may have different effects on earthquake-triggered landslides, because they have varied responses to the slip direction of the seismogenic fault or the propagating direction of seismic waves (Xu et al., 2014c). Probably, there are differences in vegetation covers, sunlight and evaporations, precipitations, and soil conditions on different slope aspects (Kamp et al., 2008; Yalcin, 2008). The slope aspects in the study are divided into nine kinds, i.e. flat, north (N), northeast (NE), east (E), southeast (SE), south (S), southwest (SW), west (W), and northwest (NW). The slope aspect of SE has the largest area: 923 km^2, accounting for 17.1% of the entire study area (Fig. 6c). The slope aspect of SW has the largest *LAA* and *LVA* (4.08‰ and 9.52 mm), whereas the maximum *LNA* occurred at the slope aspect of NE (3.27 km^{-2}). Different from several other earthquakes such as the 2008 Wenchuan (Huang and Li, 2009; Xu et al., 2014b), 2010 Haiti (Xu et al., 2014c), and 2010 Yushu (Xu and Xu, 2014a) earthquakes, no single slope aspect had an absolutely high landslide abundance for the Lushan earthquake. A possible reason is that the Lushan earthquake was generated by a blind reverse fault (X.W. Xu et al., 2013a). A comparison of coseismic landslides triggered by blind fault earthquakes and surface rupture events shows that the former may trigger abundant landslides in a larger area (Xu, 2014b), which may make the slope aspect effect less obvious.

Slope position influenced coseismic landslides in several other earthquakes (Xu et al., 2012d, 2014b, 2014c, 2014d; Gorum et al., 2013; Xu and Xu, 2014a). In this study, this factor is classified into six groups (ridges, upper slopes, middle slopes, flat slopes, lower slopes, and valleys) following Weiss (2001) and Jenness et al. (2013). Fig. 6a shows ridges and valleys registered the highest landslide abundances, whereas the flat slope has lowest landslide abundances. The maximum *LNA*, *LAA*, and *LVA* are 3.81 km^{-2}, 4.62‰, and 9.99 mm in valleys, followed by ridges, which are 3.73 km^{-2}, 3.86‰, and 8.53 mm (Fig. 6d). High landslide abundance at ridges is probably due to the seismic wave amplification effect on steep topography and isolated rocks with high susceptibility to coseismic landslides (Meunier et al., 2008; Xu et al., 2014d). Valleys may be unstable because of incision by rivers or accumulated loose and weathered deposits (Xu et al., 2014c). Nonetheless, due to the largest areal coverage (3,426 km^2, 63.5%), the maximum landslide number, area, and volume values fall in the class of middle slopes, which are 9743 pieces, 11.95 km^2, and 26.78 × 10^6 m^3, or 62.7%, 64.5%, and 64.9 % of the total, respectively. Such a coseismic landslide distribution is similar to several other previous events, including the 2008 Wenchuan (Xu et al., 2014b), 2010 Yushu (Xu and Xu, 2014a), and 2010 Haiti (Xu et al., 2014c) earthquakes. However, the overall correlations between the slope positions and the landslide abundances are also different from previous studies (Gorum et al., 2013; Xu et al., 2014b, 2014c, 2014d). Unlike the clear relationship between coseismic landslides and slope angle, the correlations between slope position and coseismic landslides may change with topographic, geologic, and seismic conditions.

Coseismic landslides often occur along drainages (Xu and Xu, 2014a; Xu et al., 2014c). To analyze this, we constructed 11-class buffers from drainages with a 200 m interval. The maximum *LNA*, *LAA*, and *LVA* occur at 0–200 m distances from drainages, which are 5.79 km^{-2}, 6.97‰, and 14.58 mm, respectively (Fig. 6e). Landslide abundances generally decrease with increasing distance from the drainage, except for the distance greater than 2,000 m. The slope position and distance from drainages have somewhat similar meanings (Xu et al., 2014c). Ridges generally have long distance from drainages, thus the area of over 2,000 m distant from drainages has higher landslide abundances.

4.2.2. Geologic factors

Lithology is generally considered as an important factor of landslide occurrence, for both earthquake-triggered and non-seismic ones. In the study area, the lithology classes of Cretaceous (K), Devonian (D), and

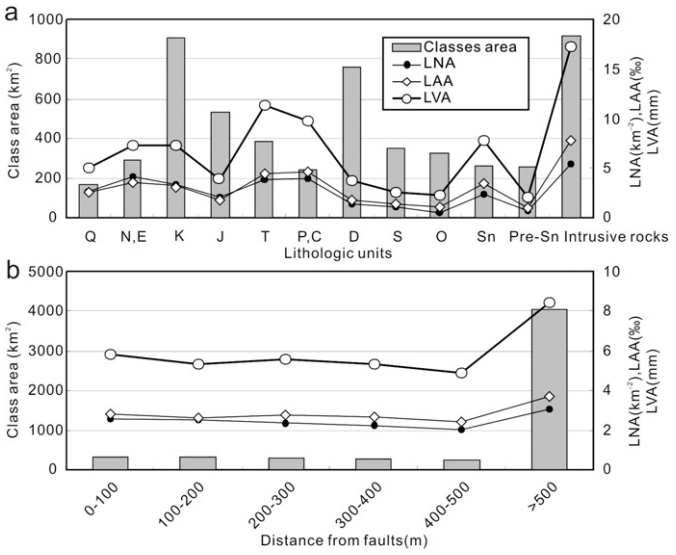

Fig. 7. Correlations of geologic factors with landslide abundance proxies. a) generalized lithology combinations; b) distance from faults.

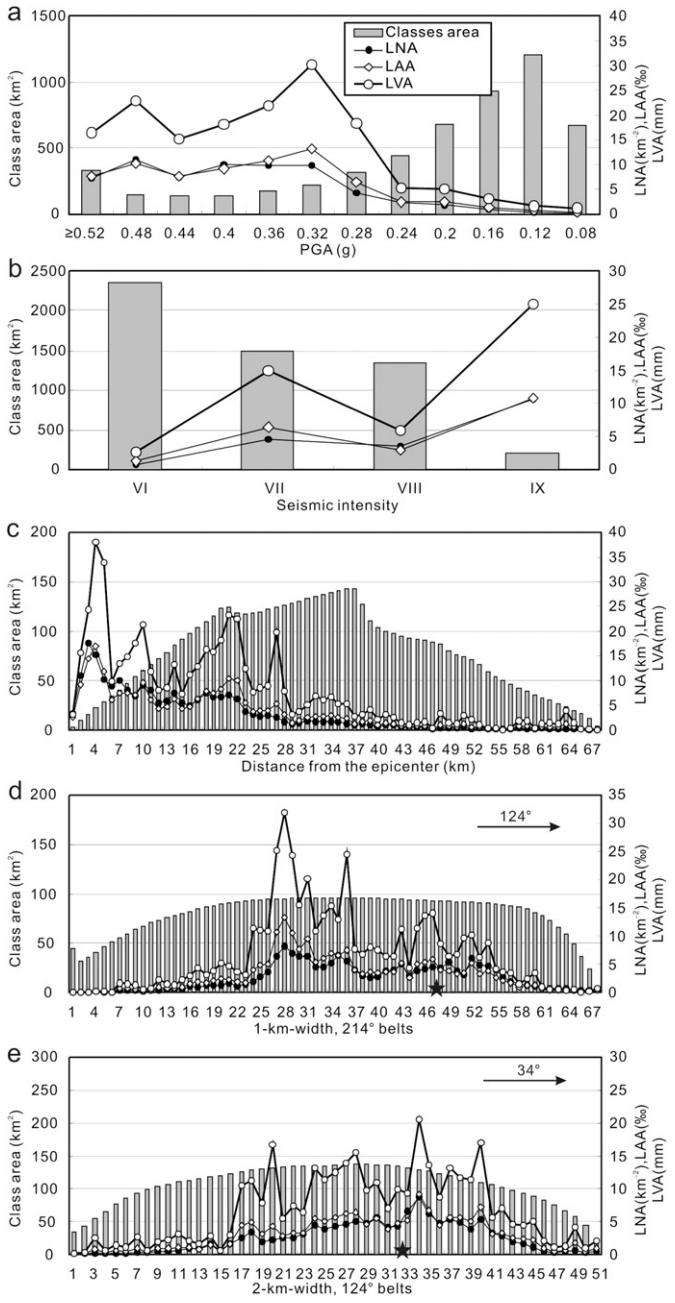

Fig. 8. Correlations of seismic factors with landslide abundance proxies. a) PGA; b) seismic intensity, c) distance from the epicenter (30.3°N, 103°E); d) distance from the probable seismogenic fault (214° belts); e) distance along the probable seismogenic fault (124° belts). The star in (d) and (e) represents the location of the epicenter.

intrusive rocks cover the largest areas, which are 906, 760, and 917 km^2, or 16.8%, 14.1%, and 17%, respectively. The class of intrusive rocks has the highest *LNA*, *LAA*, and *LVA* values, which are 5.38 km^{-2}, 7.78‰, and 17.25 mm, respectively (Fig. 7a). Such a phenomenon is also observed in the Wenchuan earthquake-triggered landslides (Xu et al., 2014b), probably because many intrusive rocks crops out along the Longmenshan fault, and the movement of the fault would have weakened the strength of these rocks. Similar tectonic weakening effects have also been noticed in previous studies (Kellogg, 2001; Fisher, 2003; Korup, 2004; Osmundsen et al., 2009; Shroder and Weihs, 2010).

Distance from faults or lineaments is often used in non-seismic landslide susceptibility assessments (Yilmaz, 2009; Demir et al., 2013; Pourghasemi et al., 2013), and it is considered that landslide abundances generally decrease with increasing distance from faults. We extracted faults in the study area from the three sheets of 1:200,000 geologic maps. We divided six classes of distance from faults in 100 m belts. The result shows no clear correlation between them and even an opposing tendency is observed (Fig. 7b). All the maximum *LNA*, *LAA*, and *LVA* occur at distances over 500 m from faults, which are 3.06 km^{-2}, 3.7‰, and 8.41 mm, respectively. The possible reason is that coseismic landslides are controlled by the seismogenic faults rather than other faults in the area. We also noticed that the class of > 500 m distance from faults covers the largest area, which is 4,024 km^2 or 74.6% of the whole study area. The large differences among the areas of these classes of distances from faults probably resulted in a low statistical significance.

4.2.3. Seismic factors

We selected *PGA*, seismic intensity, distance from the epicenter, distance from the probable seismogenic fault, and distance along the fault to carry out statistical analysis of the coseismic landslides. Generally, PGA is one of the most important factors related to earthquake-triggered landslides, as in the cases of the 1999 Chi-Chi (Liao and Lee, 2000; Wang et al., 2002), 2008 Wenchuan (Xu et al., 2014b), 2010 Yushu (Xu and Xu, 2014a), 2010 Haiti (Xu et al., 2012d, 2014c; Gorum et al., 2013), and 2013 Minxian (Xu et al., 2014d) earthquakes. Coseismic landslide abundances generally increase with *PGA* values. The *PGA* data of the Lushan earthquake were downloaded from the US Geological Survey (US Geological Survey, 2013), which were prepared by a combination of records from several seismic stations and a simulation-based method. The range of *PGA* for the study area is from 0.08 to 0.58 g with a 0.04 g interval. Although the curves in Fig. 8a do not show a rigorous positive correlation between *PGA* values and the coseismic landslides, the landslide abundance values in classes of *PGA* ≥ 0.2 g are much higher than those in lower PGA classes (Fig. 8a). The total area of the PGA classes of ≥ 0.2 g covers 2,591 km^2, and only accounts for about 48% of the total. However, the total number, area, and volume of the coseismic landslides occurring in this area are 13,862 pieces, 16 km^2, and 35.65×10^6 m^3, or about 89.2%, 86.3%, and 86.4% of the total, respectively.

The seismic intensity information of the study area was extracted from the "Seismic Intensity Map of the 2013 Lushan Earthquake" produced by the China Earthquake Administration (CEA, 2013; Fig. 2). The areas of the seismic intensity zones increase with the decreasing seismic intensity (Fig. 8b). In general, *LNA*, *LAA*, and *LVA* increase as the seismic intensity increases except for the VIII zone, probably due

to the area near the Baoxing County, located in the VII zone but with a steep topography and thus higher landslide susceptibility. The maximum landslide abundances occur in the IX zone, which are 10.72 km^{-2}, 10.77‰, and 25.02 mm, respectively.

We also constructed 68 buffers with 1 km distance intervals from the epicenter (30.3°N, 103°E). The outer belts were truncated where they intersect with the boundary of the study area. Generally, the landslide abundance values of the areas 40 km or less from the epicenter are much higher than other areas (Fig. 8c). Although the largest distance of a landslide from the epicenter is about 68 km, the area of 0–40 km distance registers most landslides: 14,827 in number, 17.41 km^2 in area, and 38.82 × 10^6 m^3 in volume, or 95.4%, 94%, and 94.1% of the total, respectively.

The seismogenic fault is considered to play a very important role in inducing earthquake-triggered landslides. Coseismic landslides were strongly controlled by seismogenic faults in many earthquake events, such as the 2002 Denali, Alaska (Harp et al., 2003; Jibson et al., 2004b; Gorum et al., 2014), 2008 Wenchuan (Gorum et al., 2011; Xu et al., 2014b), 2010 Yushu (C. Xu et al., 2013d; Xu and Xu, 2014a), and 2013 Minxian (Xu et al., 2014d) earthquakes. Although coseismic landslides are usually distributed along seismogenic faults, such a relationship does not always hold, with obvious exceptions such as the 1994 Northridge (Jibson and Harp, 1994; Harp and Jibson, 1996), the Aysén Fjord, Chile (Sepúlveda et al., 2010), and the 2004 Mid-Niigata, Japan (Sato et al., 2005) earthquakes. In addition, in quite a few events including the 1999 Chi-Chi (Liao and Lee, 2000; Wang et al., 2002), 2005 Kashmir (Sato et al., 2007) and 2007 Lorca, Spain (Alfaro et al., 2012), most of the coseismic landslides occurred on the hanging walls and were distributed along the seismogenic faults, but were not directly controlled by the seismogenic faults. Therefore, we analyzed the correlations between coseismic landslide abundance values with distance from or along the probable seismogenic fault. The correlation with distance from the seismogenic fault may represent the controlling ability of the fault over the landslides, while that with distance along the fault may reflect the controlling intensity in different segments of the fault. As the Lushan earthquake was presumably generated by a blind reverse fault (X.W. Xu et al., 2013a), and the exact location and ground projection of the fault is unknown yet, we estimate the parameters of this fault from the focal mechanism solutions reported by several institutes (e.g. http://www.globalcmt.org and http://earthquake.usgs.gov, et al.) and researchers (C.L. Liu et al., 2013; Hu and Jiang, 2013; J. Liu et al., 2013; Lin et al., 2013; Lv et al., 2013; Wang et al., 2013; Xie et al., 2013; Zeng et al., 2013). Combining these data with local geologic setting, the strike directions of the probable seismogenic fault are in the range of 198°–222°, mostly 210°–220°. Therefore, an approximate average value of 214° was selected as the strike direction of the probable seismogenic fault of the Lushan earthquake. The epicenter (30.3°N, 103°E) was selected as the original point to construct belts that are parallel or perpendicular to the probable seismogenic fault. In other words, two groups of belts that strike in 214° and 124° were constructed. Considering the shape of the study area, the width of the 214° belts is set to be 1 km, whereas the width of the 124° belts was set to be 2 km. The 214°-trending 1-km-width belts were numbered from northwest to southeast as 1 to 68 (Fig. 8d) and the epicenter is located between the belts 47 and 48. The landslide abundances in the belts 24–54 are much higher than those in other areas (Fig. 8d). This 31 km wide, northeast-southwest trending area registers most of the coseismic landslides: 13,104 in number, 15.88 km^2 in area, and 35.93 × 10^6 m^3 in volume, or 84.3%, 85.7%, and 87.1% of the total, respectively. The 124° 2-km-width belts from southwest to northeast were numbered 1 to 51 (Fig. 8e) and the epicenter is located between the belts 32 and 33. The landslide abundances in areas of the belts 17–45 (29 belts) are much higher than those in other areas (Fig. 8e). This 58 km wide, northwest-southeast trending area registers most of the coseismic landslides: 14,461 in number, 17.02 km^2 in area, and 38.01 × 10^6 m^3 in volume, or 93%, 91.9%, and 92.1% of the total, respectively.

5. Discussion

5.1. Lithology, topography, and coseismic landslides

Lithology and slope angle are considered to play important roles in occurrence of landslides, including both earthquake-triggered and non-seismic ones. It is generally accepted that the steeper the topography, or the lower the rock strength, the higher the probability of earthquake-triggered landslides. However, the areas where hard rocks crop out generally have steeper topography than trhe areas with soft rocks. Thus, on a regional scale, the rock strength and slope angle may be a couple of contradictory factors affecting landslide occurrence. However, several previous studies (Korup, 2008; Korup and Schlunegger, 2009; Clarke and Burbank, 2010) pointed out that information of regional slope angle in selected homogeneous rock types can be used as a proxy for landslide susceptibility. Landslides tend to occur on slopes inclined slightly steeper (Gorum et al., 2013). The peaks of distributions of slope angle are used as the information proxy of slope angle on regional scales (Korup, 2008; Korup and Schlunegger, 2009; Gorum et al., 2013). In order to comprehensively explore the correlations between the two contradictory factors for coseismic landslide occurrence, both peak and mean values of slope angle, *LAA* in generalized

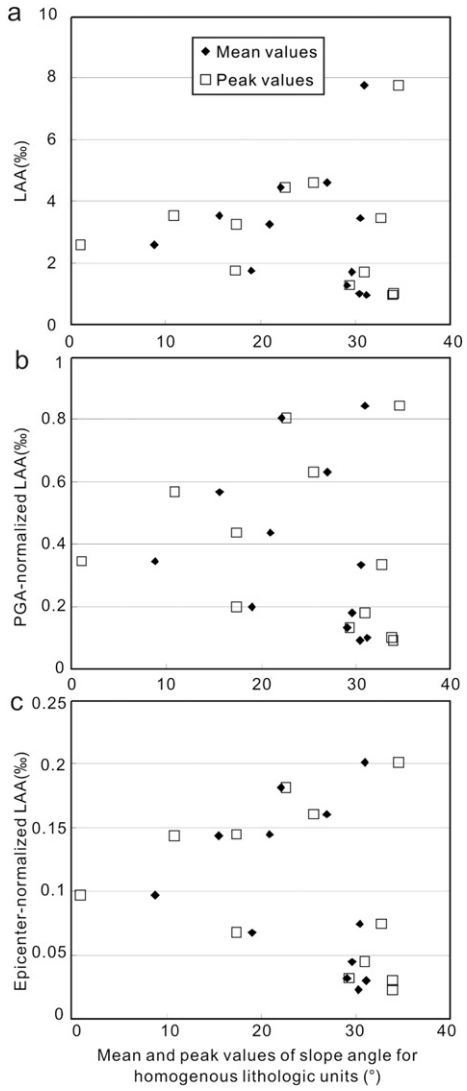

Fig. 9. Scatter plots of slope angle (mean and peak values) with landslide area abundance in the 12 generalized homogeneous lithology combinations. a) original LAA value; b) PGA normalized LAA value; c) Epicenter distance normalized LAA value.

homogeneous lithology combinations were calculated (Table 1) and the values were plotted (Fig. 9a). Unlike previous studies, these points are unexpectedly very scattered, and there is no clear relationship between the mean or peak values of slope angle and landslide area abundance for generalized homogeneous lithology combinations (Fig. 9a). It should be noted that most of the previous studies on this issue (Korup, 2008; Korup and Schlunegger, 2009; Clarke and Burbank, 2010) did not focus on landslides triggered by an individual earthquake. Compared with historical or pre-historical landslides on regional scales, landslides triggered by an individual earthquake were not only affected by slope and lithology type, but also strongly affected by earthquake sources. Therefore, we normalized the landslide area abundance values by *PGA* values and distance from the epicenter. The method for normalizing is to take the mean and peak values divided by the *PGA* values (the real values from 0.08 g to ≥ 0.52 g are substituted by the class number from 1 to 12) or the distance from the epicenter in homogeneous lithology types. In this way, we can eliminate the effects of the earthquake sources on *LAA* in homogeneous lithology types. However, the resulting points are still very scattered, without any obvious correlations (Fig. 9b,c). Therefore, we suggest that although the information of slope angle of homogeneous lithology types can represent the rock strength, it may not represent the landslide susceptibility of the lithology type.

5.2. Imbricated reverse and/or thrust seismogenic faults and coseismic landslides

There are many similarities between the 2008 Wenchuan and 2013 Lushan earthquakes. Both occurred on northeast-striking faults of the Longmenshan thrust zone; the topography of the earthquake affected areas of both events is very steep, and the seismogenic faults of both events are dominated by reverse motion. However, the spatial distribution patterns of coseismic landslides triggered by the two events are quite different. For the 2008 Wenchuan earthquake, most of coseismic landslides are concentrated along the seismogenic fault, mostly in the hanging wall of the fault (Xu et al., 2014b). Overall, the seismogenic fault of the Wenchuan earthquake can be considered as a linear core of the energy released during the earthquake, and the coseismic landslide abundance generally decreases with increasing distance from the seismogenic fault. However, the Lushan earthquake occurred likely on a blind reverse fault that did not rupture to the surface (X.W. Xu et al., 2013a). Xu (2014b) constructed two simple models to illustrate the differences in spatial patterns of landslides triggered by earthquakes on reverse faults with or without surface ruptures. For those with surface ruptures such as the 2008 Wenchuan earthquake, the hanging wall is characterized by strong ground shaking and significant deformation in a small area near the seismogenic fault, thus the coseismic landslides are distributed along and near the fault, mostly on the hanging wall. For earthquakes produced by blind faults such as the 2013 Lushan earthquake, the coseismic deformation, which is an important factor for coseismic landslides (Moro et al., 2007), would be absorbed by the overlying crust in a large area. Therefore, the landslides triggered by such earthquakes are generally quite dispersed.

The Longmenshan thrust zone is characterized by a series of imbricated reverse or thrust faults. During major earthquakes, more than one fault may rupture. For example, during the 2008 Wenchuan earthquake, although most of the energy is released by the rupture of the Yingxiu-Beichuan fault, the Guanxian-Jiangyou fault also ruptured (Fig. 2). As a result, whereas most of the coseismic landslides occurred in the hanging wall of the Yingxiu-Beichuan fault, many landslides also took place in the area between the two faults (the hanging wall of the Guanxian-Jiangyou fault but the footwall of the Yingxiu-Beichuan fault). The seismogenic fault of the Lushan earthquake is a northeast-striking blind reverse fault. The major northeast-striking Shuangshi-Dachuan fault may also release part of the energy because a series of tensional ground fissures, landslides, bedrock collapses and liquefactions occurred near the fault (X.W. Xu et al., 2013a; Xu and Xu, 2014b). Similar to the Wenchuan event, the spatial distribution of the Lushan earthquake-triggered landslides can be explained using the spatial distribution of the structures in the affected area. The energy may have been released not only by the blind reverse seismogenic fault (X.W. Xu et al., 2013a), but also by the neighboring Shuangshi-Daichuan fault (Xu and Xu, 2014b), as well as other sub-faults parallel to the seismogenic fault in the vicinity.

Besides the 2008 Wenchuan earthquake and the 2013 Lushan earthquake, the 1999 Chi-Chi earthquake also shows similarity of the fault structure, topography, and coseismic landslides. The Chelungpu fault, the seismogenic fault of the Chi-Chi event, ruptured the surface for over 90 km (Chen et al., 2001; Lee et al., 2002). Most of the coseismic landslides, however, occurred in the area between the Shuangtung, Shuilikeng, and Lishan faults (Liao and Lee, 2000; Wang et al., 2002), which form a typical imbricated fold-and-thrust belt together with the Chelungpu fault. Although these faults did not rupture during the earthquake, they may also contribute to the coseismic landslide occurrence by absorbing seismic energy (Wang et al., 2000) or releasing stress.

Based on the correlations between the regional tectonics and the coseismic landslides related to the three earthquakes (Wenchuan, Lushan, and Chi-chi), we suggest that earthquakes that occurred on an imbricated reverse fault system may be affected by multiple sub-faults, and therefore the coseismic landslides would occur along the imbricated fault belt, rather than only one sub-fault (Fig. 10). The spatial distribution patterns of coseismic landslides would be affected by the differences of earthquake energy release on different sub-faults of the imbricated reverse fault system.

5.3. Landslide triggering ability of the blind reverse fault during the Lushan earthquake

The coseismic landslide distribution area is often used to measure the landslide triggering ability of an earthquake. Here the correlation between earthquake magnitudes and distribution areas of coseismic landslides of earthquakes worldwide is presented (Fig. 11), where the solid and dashed lines are the two upper margins determined by Keefer (1984) and Rodriguez et al. (1999). Almost all earthquakes are located under the dashed line from Rodriguez et al. (1999) except for the 1988 Saguenay, Canada, Mw 5.8 earthquake and the 2008 Wenchuan, China, Mw 7.9 earthquake, with earthquake-triggered landslides distribution areas of 45,000 km^2 (Rodriguez et al., 1999) and 110,000 km^2 (Xu et al., 2014b), respectively. The coseismic landslide distribution area related to the Lushan earthquake is about 5,400 km^2. This event is located beneath, but very close to the upper margin drawn by Keefer (1984). Although the point of the Lushan event is beneath the two proposed upper margins, the area is larger than the most of the earthquakes with similar magnitudes. However, the absolute value of coseismic landslide distribution area related to an earthquake is difficult to obtain, since sometimes there will be a few coseismic landslides on high landslide susceptibility slopes very far away from the earthquake source (Alfaro et al., 2012; Jibson and Harp, 2012; Xu et al., 2014b,d).

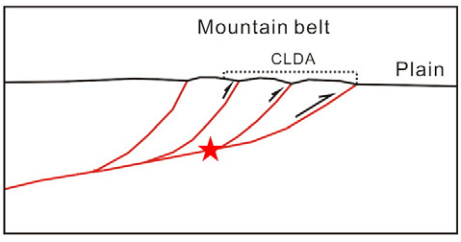

Fig. 10. Schematic model illustrating the distribution of landslides triggered by earthquakes on imbricated reverse and thrust faults. CLDA: Coseismic landslide-distribution area.

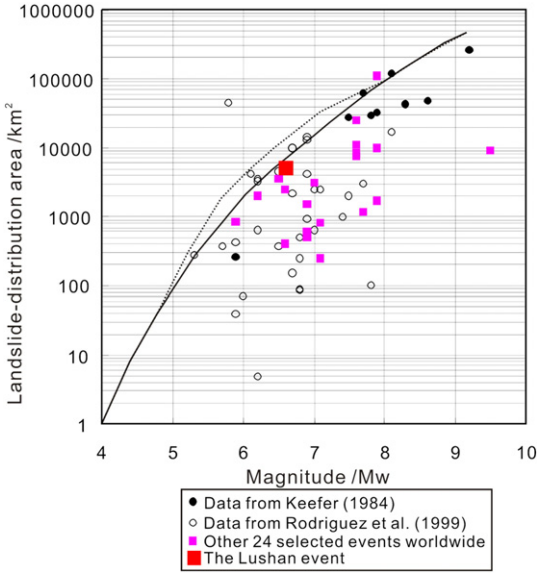

Fig. 11. Correlations between earthquake magnitudes (Mw) and distribution areas of coseismic landslides worldwide. Data from Keefer (1984) are from earthquake events occurred before 1980, and from Rodriguez et al. (1999) are from earthquake events occurred from 1980 to 1997. The data of other 24 select events worldwide are collected from the 1908 Messian earthquake (Murphy, 1995) to the 2013 Minxian-Zhangxian earthquake (Xu et al., 2014d), which is supplementary to the data from Keefer (1984) and Rodriguez et al. (1999). The dashed line is from Rodriguez et al. (1999) and the solid line is from Keefer (1984).

Therefore, the landslide area and landslide number are also used to compare the landslides triggered by the Lushan earthquake with those by other earthquakes. The published information of landslide area related to individual earthquakes is much less than the landslide distribution area. We collected the data of 13 earthquakes from the literature (Harp et al., 1984; Pearce and O'Loughlin, 1985; Harp and Jibson, 1995; Murphy, 1995; Liao and Lee, 2000; Jibson et al., 2004b; Sato et al., 2005, 2007; Wang et al., 2007; Kamp et al., 2008; Yagi et al., 2009; Sepúlveda et al., 2010; Gorum et al., 2014) and our previous studies (Xu, 2014a, 2014b; Xu and Xu, 2014a; Xu et al., 2014b, c, d) (Fig. 12). Then, we correlated the total landslide areas with earthquake magnitudes based on these 13 individual earthquake events, such as the 1929 Murchison, New Zealand, Mw 7.7 earthquake (Pearce and O'Loughlin, 1985) and the 2013 Minxian, China, Mw 5.9 earthquake (Xu et al., 2014d). The points are drawn and the power-law regression curve is produced using the least square method (Fig. 12a). The curve has an R^2 value of 0.6914. The point for the Lushan earthquake-triggered landslides is above the regression curve. Based on the line, the coseismic landslide area related to an Mw 6.6 earthquake should be about 10 km^2, which is about half of the actual landslide area (18.88 km^2) related to the Lushan earthquake. The correlation between the landslide number and earthquake magnitudes is also shown (Fig. 12b). The number of the landslides (area ≥ 100 m^2, 15,546 pieces) triggered by the Lushan earthquake is also above the regression line from the 13 events. However, the regression is not very good, with R^2 only 0.1931. This is likely because the landslide number may differ significantly among landslide inventory maps prepared by different interpreters, since a coalescing landslide may be considered as either a single landslide or several landslides, whereas no such differences would occur to the landslide area (Xu, 2014b). In addition, Keefer (1994) proposed a regression relationship between the seismic moment (M_o) and the total volume (V) of landslides related to an individual earthquake as

$$V = M_o/10^{18.9\pm0.13} \quad (1)$$

where M_o is measured in dyne cm^{-1} and V is in m^3. The correlation has been applied to several studies, such as Parise (2000), and also been used to compare results from the formula with actual landslide volumes from detailed landslide databases related to individual earthquakes, such as the 2010 Haiti event (Xu et al., 2014c). The seismic moment of the Lushan earthquake is 1.02×10^{26} dyne cm^{-1} (Global Centroid Moment Tensor Catalog, http://www.globalcmt.org/CMTsearch.html, last accessed in July 2014). Based on the regression formula, the total coseismic landslide volume of the Lushan earthquake can be calculated as 12.84×10^6 m^3 (9.52×10^6 – 17.32×10^6 m^3). The volume calculated from our detailed coseismic landslide inventory and the "area to volume" scaling relationship (Larsen et al., 2010) suggest the volume of landslides triggered by the Lushan earthquake is 41.56×10^6 m^3, which is about three times that from the regression formula (Keefer, 1994). Therefore, the distribution area, areal area, number, and volume of the landslides triggered by the Lushan earthquake are higher than the values from most of earthquakes with similar magnitudes or calculated by the regression formula. This indicates the Lushan earthquake has higher landslide triggering ability. We infer that the blind reverse seismogenic fault (Xu, 2014b), the imbricated structure in the

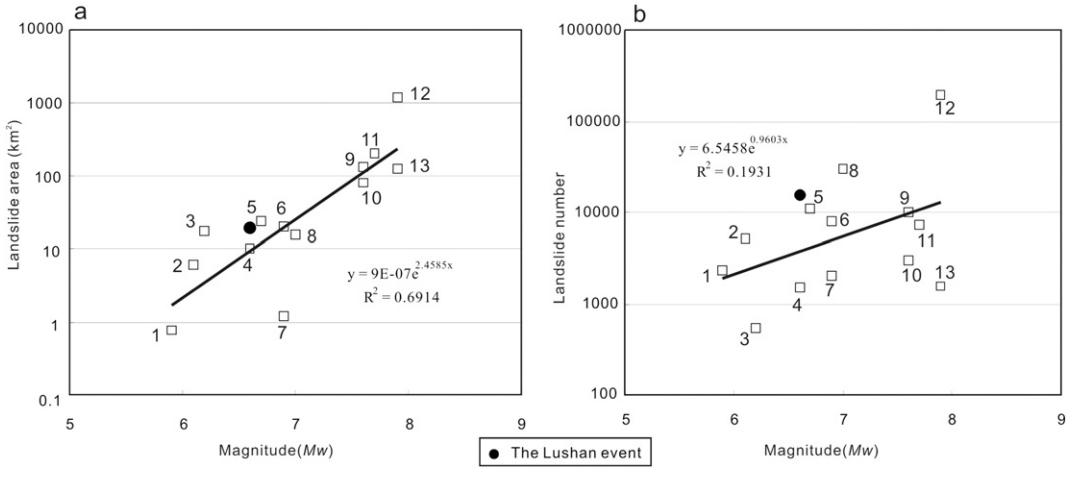

Fig. 12. Correlations of earthquake magnitude with coseismic landslides related to 13 individual earthquake events. a) landslide area; b) landslide number. 1, Mw 5.9 Minxian-Zhangxian, China, of 2013 (Xu et al., 2014d); 2, Mw 6.1 Mammoth Lakes, USA, of 1980 (Harp et al., 1984; Xu, 2014a); 3, Mw 6.2 Aysén Fjord, Chile, of 2007 (Sepúlveda et al., 2010); 4, Mw 6.6 Mid-Niigata, Japan, of 2004 (Sato et al., 2005; Wang et al., 2007; Xu, 2014b); 5, Mw 6.7 Northridge, USA, of 1994 (Harp and Jibson, 1995); 6, Mw 6.9 Iwate-Miyagi Nairiku, Japan, of 2008 (Yagi et al., 2009; Xu, 2014b); 7, Mw 6.9 Yushu, China, of 2010 (Xu and Xu, 2014a); 8, Mw 7.0 Port-au-Prince, Haiti, of 2010 (Xu, 2014b; Xu et al., 2014c); 9, Mw 7.6 Chi-Chi, Taiwan, of 1999 (Liao and Lee, 2000); 10, Mw 7.6 Kashmir of 2005 (Sato et al., 2007; Kamp et al., 2008; Xu, 2014b); 11, Mw 7.7 Murchison, New Zealand, of 1929 (Pearce and O'Loughlin, 1985); 12, Mw 7.9 Wenchuan, China, of 2008 (Xu et al., 2014b); 13, Mw 7.9 Denali, Alaska, USA, of 2002 (Jibson et al., 2004b; Gorum et al., 2014).

earthquake source area, the steep and rugged topography, and a fractured and densely jointed lithology resulted from prolonged tectonic activity all contribute to the large amount of the Lushan earthquake-triggered landslides.

6. Conclusions

In this study, we compiled the first detailed inventory of 22,528 landslides triggered by the 2013 Lushan, China Mw 6.6 earthquake. These coseismic landslides are distributed in a nearly ellipse area of about 5,400 km^2, with a horizontal projection area of 18.88 km^2 and a total volume of 41.56×10^6 m^3. The major axis of this ellipse is in northeast direction, consistent with the striking direction of the presumable seismogenic fault. Correlation analysis between coseismic landslides and topographic, geologic, and seismic factors was performed for the 14,580 landslides of area ≥100 m^2. The results show that the elevations ranging from 1,000 to 1,500 m a.s.l. have the highest landslide abundance values. The landslide abundance increases with slope angle. Although the effect of slope aspect on these landslides is less obvious, the maximum landslide number, area, and volume occur at the southeast slope aspect, which is similar to the 2008 Wenchuan earthquake-triggered landslides. Ridges and valleys are loci with relatively higher landslide abundances. Areas with intrusive underlying bedrocks register the highest landslide abundances. There are no obvious correlations between coseismic landslides and distance from faults as previously suggested. Most of the coseismic landslides occurred in the areas of *PGA* values ≥0.2 g or within 40 km distance around the epicenter. Correlations between coseismic landslide abundances and the probable seismogenic fault show that the coseismic landslides are generally concentrated within a 31×58 km^2 rectangle area with a long axis trending northeast. This result can assist future hazard assessment, mitigation, and prevention of landslides and debris flows of the earthquake struck area. In addition, the Lushan earthquake shows a higher ability of triggering landslides compared with other quakes of similar magnitudes. This suggests that the empirical correlations between earthquake magnitude and coseismic landslide may need to be modified based on recently published detailed coseismic landslide inventory maps, such as those related to the 2008 Wenchuan, 2010 Haiti, and 2010 Yushu earthquakes. It is clear that more accurate and detailed individual earthquake event-based landslide inventory maps or databases are warranted to facilitate better understanding of the topographic, geologic, and seismic factors that control coseismic landslides.

Acknowledgments

This research was supported by the National Natural Science Foundation of China (41472202, 41202235, 91214201) and the National Science Council (NSC, now Ministry of Science and Technology) of Taiwan (102-2811-M-002-063 and 102-2628-M-002-007-MY3). Comments from Takashi Oguchi (Editor), Christopher Gomez, and other anonymous reviewers improved this manuscript. We are grateful for the Institute of Remote Sensing and Digital Earth, Chinese Academy of Sciences, for providing most of the high resolution post-earthquake aerial photographs and pre-earthquake satellite images. We are also grateful for the Sichuan Bureau of Surveying, Mapping and Geoinformation and the Institute of Optics and Electronics, Chinese Academy of Sciences, for providing aerial photographs. We thank the China Center for Resources Satellite Data and Application for the support of the ZY-3 images.

Appendix A. Supplementary data

Supplementary data associated with this article can be found in the online version, at doi: http://dx.doi.org/10.1016/j.geomorph.2015.07.002. These data include Google maps of the most important areas described in this article.

References

Agnesi, V., Camarda, M., Conoscenti, C., Maggio, C.D., Diliberto, I.S., Madonia, P., Rotigliano, E., 2005. A multidisciplinary approach to the evaluation of the mechanism that triggered the Cerda landslide (Sicily, Italy). Geomorphology 65 (1–2), 101–116.

Alfaro, P., Delgado, J., García-Tortosa, F.J., Lenti, L., López, J.A., López-Casado, C., Martino, S., 2012. Widespread landslides induced by the Mw 5.1 earthquake of 11 May 2011 in Lorca, SE Spain. Eng. Geol. 137–138, 40–52.

Árnadóttir, T., Segall, P., 1994. The 1989 Loma Prieta earthquake imaged from inversion of geodetic data. J. Geophys. Res. Solid Earth (1978–2012) 99 (B11), 21835–21855.

Arne, D., Worley, B., Wilson, C., Chen, S.F., Foster, D., Luo, Z.L., Liu, S.G., Dirks, P., 1997. Differential exhumation in response to episodic thrusting along the eastern margin of the Tibetan Plateau. Tectonophysics 280 (3), 239–256.

Basharat, M., Rohn, J., Baig, M.S., Khan, M.R., 2014. Spatial distribution analysis of mass movements triggered by the 2005 Kashmir earthquake in the Northeast Himalayas of Pakistan. Geomorphology 206, 203–214.

Bozzano, F., Martino, S., Naso, G., Prestininzi, A., Romeo, R.W., Mugnozza, G.S., 2004. The large Salcito landslide triggered by the 2002 Molise, Italy, earthquake. Earthquake Spectra 20 (S1), S95–S105.

Burchfiel, B.C., Royden, L.H., van der Hilst, R.D., Hager, B.H., Chen, Z., King, R.W., Li, C., Lü, J., Yao, H., Kirby, E., 2008. A geological and geophysical context for the Wenchuan earthquake of 12 May 2008, Sichuan, People's Republic of China. GSA Today 18 (7), 4–11.

Calais, E., Freed, A., Mattioli, G., Amelung, F., Jónsson, S., Jansma, P., Hong, S.-H., Dixon, T., Prépetit, C., Momplaisir, R., 2010. Transpressional rupture of an unmapped fault during the 2010 Haiti earthquake. Nat. Geosci. 3 (11), 794–799.

CEA, 2013. Seismic Intensity Map of the 2013 Lushan Earthquake released on Arpil 25, 2013, http://www.cea.gov.cn/publish/dizhenj/468/549/20130503105353814752350 (in Chinese).

Chang, M., Tang, C., Li, W.L., Zhang, D.D., Jia, T., Ma, G.C., Zhou, Z.Y., 2013. Image interpretation and spatial analysis of geohazards induced by "4.20" Lushan earthquake in epicenter area. J. Chengdu Univ. Technol. (Sci. Technol. Ed.) 40 (3), 275–281 (in Chinese).

Chen, S.F., Wilson, C.J.L., Deng, Q.D., Zhao, X.L., Luo, Z.L., 1994. Active faulting and block movement associated with large earthquakes in the Min Shan and Longmen Mountains, northeastern Tibetan Plateau. J. Geophys. Res. Solid Earth (1978–2012) 99 (B12), 24025–24038.

Chen, Z., Burchfiel, B.C., Liu, Y., King, R.W., Royden, L.H., Tang, W., Wang, E., Zhao, J., Zhang, X., 2000. Global Positioning System measurements from eastern Tibet and their implications for India/Eurasia intercontinental deformation. J. Geophys. Res. Solid Earth (1978–2012) 105 (B7), 16215–16227.

Chen, Y.-G., Chen, W.-S., Lee, J.-C., Lee, Y.-H., Lee, C.-T., Chang, H.-C., Lo, C.-H., 2001. Surface rupture of 1999 Chi-Chi earthquake yields insights on active tectonics of central Taiwan. Bull. Seismol. Soc. Am. 91 (5), 977–985.

Chen, L.C., Ran, Y.K., Wang, H., Li, Y.B., Ma, X.Q., 2013. The Lushan Ms7.0 earthquake and activity of the southern segment of the Longmenshan fault zone. Chin. Sci. Bull. 58 (28–29), 3475–3482.

Chen, X.L., Liu, C.G., Yu, L., Lin, C.X., 2014a. Critical acceleration as a criterion in seismic landslide susceptibility assessment. Geomorphology 217, 15–22.

Chen, X.L., Yu, L., Wang, M.M., Lin, C.X., Liu, C.G., Li, J.Y., 2014b. Brief Communication: Landslides triggered by the Ms = 7.0 Lushan earthquake, China. Nat. Hazards Earth Syst. Sci. 14 (5), 1257–1267.

Chen, L.C., Wang, H., Ran, Y.K., Lei, S.X., Li, X., Wu, F.Y., Ma, X.Q., Liu, C.L., Han, F., 2014. The 2013 Lushan Ms 7.0 Earthquake: Varied seismogenic structure from the 2008 Wenchuan Earthquake. Seismol. Res. Lett. 85 (1), 34–39.

Chigira, M., Wu, X.Y., Inokuchi, T., Wang, G.H., 2010. Landslides induced by the 2008 Wenchuan earthquake, Sichuan, China. Geomorphology 118 (3–4), 225–238.

Clark, M.K., Royden, L.H., 2000. Topographic ooze: Building the eastern margin of Tibet by lower crustal flow. Geology 28 (8), 703–706.

Clarke, B.A., Burbank, D.W., 2010. Bedrock fracturing, threshold hillslopes, and limits to the magnitude of bedrock landslides. Earth Planet. Sci. Lett. 297 (3–4), 577–586.

Cook, K.L., Royden, L.H., Burchfiel, B.C., Lee, Y.H., Tan, X., 2013. Constraints on Cenozoic tectonics in the southwestern Longmen Shan from low-temperature thermochronology. Lithosphere 5 (4), 393–406.

Cui, P., Zhang, J.Q., Yang, Z.J., Chen, X.Q., You, Y., Li, Y., 2014. Activity and distribution of geohazards induced by the Lushan earthquake, April 20, 2013. Nat. Hazards 73 (2), 711–726.

Dai, F.C., Xu, C., Yao, X., Xu, L., Tu, X.B., Gong, Q.M., 2011a. Spatial distribution of landslides triggered by the 2008 Ms 8.0 Wenchuan earthquake, China. J. Asian Earth Sci. 40 (4), 883–895.

Dai, F.C., Tu, X.B., Xu, C., Gong, Q.M., Yao, X., 2011b. Rock avalanches triggered by oblique-thrusting during the 12 May 2008 Ms 8.0 Wenchuan earthquake, China. Geomorphology 132 (3–4), 300–318.

Demir, G., Aytekin, M., Akgün, A., İkizler, S.B., Tatar, O., 2013. A comparison of landslide susceptibility mapping of the eastern part of the North Anatolian Fault Zone (Turkey) by likelihood-frequency ratio and analytic hierarchy process methods. Nat. Hazards 65 (3), 1481–1506.

Deng, Q.D., Chen, S.F., Zhao, X.L., 1994. Tectonics, seismicity and dynamics of Longmenshan Mountains and its adjacent regions. Seismol. Geol. 16 (4), 389–403 (in Chinese).

Disaster Prevention Department of China Earthquake Administration, 1999. Catalog of modern earthquake of China (1912 A.D.–1990 A.D.). China Science and Technology Press, Beijing (637 pages (in Chinese)).

Disaster Prevention Department of National Seismological Bureau, 1995. Catalog of strong historical earthquake of China (23 century B.C.–1911 A.D.). Seismological Press, Beijing (514 pages (in Chinese)).

Fan, X.M., van Westen, C.J., Korup, O., Gorum, T., Xu, Q., Dai, F.C., Huang, R.Q., Wang, G.H., 2012a. Transient water and sediment storage of the decaying landslide dams induced by the 2008 Wenchuan Earthquake, China. Geomorphology 171–172, 58–68.
Fan, X.M., van Westen, C.J., Xu, Q., Gorum, T., Dai, F.C., 2012b. Analysis of landslide dams induced by the 2008 Wenchuan earthquake. J. Asian Earth Sci. 57, 25–37.
Feng, C., Liu, R., Gou, C.J., 2013. Research of landslide susceptibility after the Lushan earthquake based on Logistic regression model. J. Chengdu Univ. Technol. (Sci. Technol. Ed.) 40 (3), 282–287 (in Chinese).
Fisher, G.R., 2003. Coexistence of thrusting, extension, and opportunistic landsliding on the Berrocal fault, Los Gatos, Santa Clara County, California. 2003 Seattle Annual Meeting, Geological Society of America Abstracts with Programs, September 2003 35(6), p. 99.
Gan, W.J., Zhang, P.Z., Shen, Z.K., Niu, Z.J., Wang, M., Wan, Y.G., Zhou, D.M., Cheng, J., 2007. Present-day crustal motion within the Tibetan Plateau inferred from GPS measurements. J. Geophys. Res. Solid Earth (1978–2012) 112 (B8) (14 pages).
Gorum, T., Fan, X.M., van Westen, C.J., Huang, R.Q., Xu, Q., Tang, C., Wang, G.H., 2011. Distribution pattern of earthquake-induced landslides triggered by the 12 May 2008 Wenchuan earthquake. Geomorphology 133 (3–4), 152–167.
Gorum, T., van Westen, C.J., Korup, O., van der Meijde, M., Fan, X.M., van der Meer, F.D., 2013. Complex rupture mechanism and topography control symmetry of mass-wasting pattern, 2010 Haiti earthquake. Geomorphology 184, 127–138.
Gorum, T., Korup, O., van Westen, C.J., van der Meijde, M., Xu, C., van der Meer, F.D., 2014. Why so few? Landslides triggered by the 2002 Denali earthquake, Alaska. Quat. Sci. Rev. 95, 80–94.
Govi, M., 1977. Photo-interpretation and mapping of the landslides triggered by the Friuli earthquake (1976). Bull. Eng. Geol. Environ. 15 (1), 67–72.
Guzzetti, F., Ardizzone, F., Cardinali, M., Rossi, M., Valigi, D., 2009. Landslide volumes and landslide mobilization rates in Umbria, central Italy. Earth Planet. Sci. Lett. 279 (3–4), 222–229.
Guzzetti, F., Mondini, A.C., Cardinali, M., Fiorucci, F., Santangelo, M., Chang, K.-T., 2012. Landslide inventory maps: New tools for an old problem. Earth Sci. Rev. 112 (1–2), 42–66.
Han, Z.J., Wang, H., Wang, M.M., 2013. The surface rupture signs of the Lushan "4.20" Ms 7.0 earthquake at Longmen township, Lushan County and its discussion. Seismol. Geol. 35 (2), 388–397 (in Chinese).
Harp, E.L., Jibson, R.W., 1995. Inventory of landslides triggered by the 1994 Northridge. California earthquake (http://pubs.usgs.gov/of/1995/ofr-95-0213/plate1.gif, http://geo-nsdi.er.usgs.gov/metadata/open-file/95-213/).
Harp, E.L., Jibson, R.W., 1996. Landslides triggered by the 1994 Northridge, California, earthquake. Bull. Seismol. Soc. Am. 86 (1B), S319–S332.
Harp, E. L., Wilson, R. C., Wieczorek, G. F., 1981. Landslides from the February 4, 1976, Guatemala earthquake. Geological Survey Professional Paper 1204-A, 35 pages, 2 plates, Scale, 1:50,000. United States Government Printing Office, Washington. http://pubs.er.usgs.gov/publication/pp1204A
Harp, E. L., Tanaka, K., Sarmiento, J., Keefer, D. K., 1984. Landslides from the May 25–27, 1980, Mammoth Lakes, California, earthquake sequence. US Geological Survey Miscellaneous Investigations Series Map I-1612, Reston Va: The Survey; Denver, CO: For Sale by Branch of Distribution, Scale 1: 62,500.
Harp, E.L., Jibson, R.W., Kayen, R.E., Keefer, D.K., Sherrod, B.L., Carver, G.A., Collins, B.D., Moss, R.E.S., Sitar, N., 2003. Landslides and liquefaction triggered by the M 7.9 Denali Fault earthquake of 3 November 2002. GSA Today 13 (8), 4–10.
Harp, E.L., Keefer, D.K., Sato, H.P., Yagi, H., 2011. Landslide inventories: The essential part of seismic landslide hazard analyses. Eng. Geol. 122 (1–2), 9–21.
Hauksson, E., Jones, L.M., Hutton, K., 1995. The 1994 Northridge earthquake sequence in California: Seismological and tectonic aspects. J. Geophys. Res. Solid Earth (1978–2012) 100 (B7), 12335–12355.
Hayes, G.P., Briggs, R.W., Sladen, A., Fielding, E.J., Prentice, C., Hudnut, K., Mann, P., Taylor, F.W., Crone, A.J., Gold, R., Ito, T., Simons, M., 2010. Complex rupture during the 12 January 2010 Haiti earthquake. Nat. Geosci. 3 (11), 800–805.
Hu, X.G., Jiang, Y., 2013. Evaluation of the seismic moment of the April 20, 2013 Lushan earthquake. Earthq. Sci. 26 (3–4), 169–177.
Huang, R.Q., Li, W.L., 2009. Analysis of the geo-hazards triggered by the 12 May 2008 Wenchuan Earthquake, China. Bull. Eng. Geol. Environ. 68 (3), 363–371.
Huang, Y., Zhang, W.J., Xu, Q., Xie, P., Hao, L., 2012a. Run-out analysis of flow-like landslides triggered by the Ms 8.0 2008 Wenchuan earthquake using smoothed particle hydrodynamics. Landslides 9 (2), 275–283.
Huang, Y., Chen, W., Liu, J.Y., 2012b. Secondary geological hazard analysis in Beichuan after the Wenchuan earthquake and recommendations for reconstruction. Environ. Earth Sci. 66 (4), 1001–1009.
Jenness, J., Brost, B., Beier, P., 2013. Land facet corridor designer: Topographic position index tools. www.jennessent.com.
Jia, K., Zhou, S., Zhuang, J., Jiang, C., 2014. Possibility of the independence between the 2013 Lushan earthquake and the 2008 Wenchuan earthquake on Longmen Shan Fault, Sichuan, China. Seismol. Res. Lett. 85 (1), 60–67.
Jibson, R.W., Harp, E.L., 1994. Landslides triggered by the Northridge earthquake. Earthquakes Volcanoes 25 (1), 31–41.
Jibson, R.W., Harp, E.L., 2012. Extraordinary distance limits of landslides triggered by the 2011 Mineral, Virginia, earthquake. Bull. Seismol. Soc. Am. 102 (6), 2368–2377.
Jibson, R.W., Keefer, D.K., 1989. Statistical analysis of factors affecting landslide distribution in the new Madrid seismic zone, Tennessee and Kentucky. Eng. Geol. 27 (1–4), 509–542.
Jibson, R.W., Crone, A.J., Harp, E.L., Baum, R.L., Major, J.J., Pullinger, C.R., Escobar, C.D., Martinez, M., Smith, M.E., 2004a. Landslides triggered by the 13 January and 13 February 2001 earthquakes in El Salvador. Geol. Soc. Am. Spec. Pap. 375, 69–88.
Jibson, R.W., Harp, E.L., Schulz, W., Keefer, D.K., 2004b. Landslides triggered by the 2002 Denali fault, Alaska, earthquake and the inferred nature of the strong shaking. Earthquake Spectra 20 (3), 669–691.
Kamp, U., Growley, B.J., Khattak, G.A., Owen, L.A., 2008. GIS-based landslide susceptibility mapping for the 2005 Kashmir earthquake region. Geomorphology 101 (4), 631–642.
Keefer, D.K., 1984. Landslides caused by earthquakes. Geol. Soc. Am. Bull. 95 (4), 406–421.
Keefer, D.K., 1994. The importance of earthquake-induced landslides to long-term slope erosion and slope-failure hazards in seismically active regions. Geomorphology 10 (1–4), 265–284.
Keefer, D.K., 2000. Statistical analysis of an earthquake-induced landslide distribution —the 1989 Loma Prieta, California event. Eng. Geol. 58 (3–4), 231–249.
Keefer, D.K., 2002. Investigating landslides caused by earthquakes - a historical review. Surv. Geophys. 23 (6), 473–510.
Keefer, D.K., Wartman, J., Ochoa, C.N., Rodriguez-Marek, A., Wieczorek, G.F., 2006. Landslides caused by the M 7.6 Tecomán, Mexico earthquake of January 21, 2003. Eng. Geol. 86 (2–3), 183–197.
Kellogg, K.S., 2001. Tectonic controls on a large landslide complex: Williams Fork Mountains near Dillon, Colorado. Geomorphology 41 (4), 355–368.
Khattak, G.A., Owen, L.A., Kamp, U., Harp, E.L., 2010. Evolution of earthquake-triggered landslides in the Kashmir Himalaya, northern Pakistan. Geomorphology 115 (1–2), 102–108.
Khazai, B., Sitar, N., 2004. Evaluation of factors controlling earthquake-induced landslides caused by Chi-Chi earthquake and comparison with the Northridge and Loma Prieta events. Eng. Geol. 71 (1–2), 79–95.
Korup, O., 2004. Geomorphic implications of fault zone weakening: slope instability along the Alpine Fault, South Westland to Fiordland. N. Z. J. Geol. Geophys. 47 (2), 257–267.
Korup, O., 2008. Rock type leaves topographic signature in landslide-dominated mountain ranges. Geophys. Res. Lett. 35 (L11402) (5 pages).
Korup, O., Schlunegger, F., 2009. Rock-type control on erosion-induced uplift, eastern Swiss Alps. Earth Planet. Sci. Lett. 278 (3–4), 278–285.
Larsen, I.J., Montgomery, D.R., Korup, O., 2010. Landslide erosion controlled by hillslope material. Nat. Geosci. 3 (4), 247–251.
Lee, J.-C., Chu, H.-T., Angelier, J., Chan, Y.-C., Hu, J.-C., Lu, C.-Y., Rau, R.-J., 2002. Geometry and structure of northern surface ruptures of the 1999 Mw = 7.6 Chi-Chi Taiwan earthquake: influence from inherited fold belt structures. J. Struct. Geol. 24 (1), 173–192.
Lee, C.T., Huang, C.C., Lee, J.F., Pan, K.L., Lin, M.L., Dong, J.J., 2008. Statistical approach to earthquake-induced landslide susceptibility. Eng. Geol. 100 (1–2), 43–58.
Lei, J.S., Zhang, G.W., Xie, F.R., 2014. The 20 April 2013 Lushan, Sichuan, mainshock, and its aftershock sequence: tectonic implications. Earthq. Sci. 27 (1), 15–25.
Lei, S.X., Ran, Y.K., Wang, H., Chen, L.C., Li, X., Wu, F.Y., Han, F., Liu, C.L., 2014. Discussion on whether there are coseismic surface ruptures of the Lushan Ms 7.0 earthquake at Longmen area and its implications. Seismol. Geol. 36 (1), 266–274 (in Chinese).
Li, Z.W., Liu, S.G., Chen, H.D., Deng, B., Hou, M.C., Wu, W.H., Cao, J.X., 2012. Spatial variation in Meso-Cenozoic exhumation history of the Longmen Shan thrust belt (eastern Tibetan Plateau) and the adjacent western Sichuan basin: Constraints from fission track thermochronology. J. Asian Earth Sci. 47, 185–203.
Li, C.Y., Xu, X.W., Gan, W.J., Wen, X.Z., Zheng, W.J., Wei, Z.Y., Xu, C., Tan, X.B., Chen, G.H., Liang, M.J., Li, X.N., 2013. Seismogenic structures associated with the 20 April 2013 Ms 7.0 Lushan earthquake, Sichuan Province. Seismol. Geol. 35 (3), 671–683 (in Chinese).
Li, W.L., Huang, R.Q., Tang, C., Xu, Q., van Westen, C.J., 2013a. Co-seismic landslide inventory and susceptibility mapping in the 2008 Wenchuan earthquake disaster area, China. J. Mt. Sci. 10 (3), 339–354.
Li, W.L., Huang, R.Q., Xu, Q., Tang, C., 2013b. Rapid susceptibility mapping of co-seismic landslides triggered by the 2013 Lushan Earthquake using the regression model developed for the 2008 Wenchuan Earthquake. J. Mt. Sci. 10 (5), 699–715.
Li, G., West, A.J., Densmore, A.L., Jin, Z.D., Parker, R.N., Hilton, R.G., 2014. Seismic mountain building: Landslides associated with the 2008 Wenchuan earthquake in the context of a generalized model for earthquake volume balance. Geochem. Geophys. Geosyst. 15 (4), 833–844.
Li, Y., Zhou, R.J., Zhao, G.H., Li, H.B., Su, D.C., Ding, H.R., Yan, Z.K., Yan, L., Yun, K., Ma, C., 2014. Tectonic uplift and landslides triggered by the Wenchuan earthquake and constraints on orogenic growth: A case study from Hongchun Gully, Longmen Mountains, Sichuan, China. Quat. Int. 349, 142–152.
Li, X.Z., Kong, J.M., Cui, Y., Tian, S.J., Zhong, W., Han, P.F., Zhang, Y., 2014c. Analysis on distribution law, types and characteristics and development tendency of secondary geohazards induced by Lushan earthquake. J. Eng. Geol. 22 (2), 272–279 (in Chinese).
Liao, H.W., Lee, C.T., 2000. Landslides triggered by the Chi-Chi earthquake. Proceedings of the 21st Asian Conference on Remote Sensing, Taipei 1–2, pp. 383–388.
Lin, M.L., Wang, K.L., Kao, T.C., 2009. Landslides induced by Earthquake and their subsequent effects—lessons learned from the Chi-chi earthquake, 1999. In: Kokusho, Takaji, Tsukamoto, Yoshimichi, Yoshimine, Mitsutoshi (Eds.), Performance-Based Design in Earthquake Geotechnical Engineering: From Case History to Practice. CRC Press, pp. 287–292 (Chapter 30).
Lin, X.D., Ge, H.K., Xu, P., Dreger, D., Su, J.R., Wang, B.S., Wu, M.J., 2013. Near field full waveform inversion: Lushan magnitude 7.0 earthquake and its aftershock moment tensor. Chin. J. Geophys. 56 (12), 4037–4047 (in Chinese).
Liu, C.L., Zheng, Y., Ge, C., Xiong, X., Hsu, H.T., 2013. Rupture process of the Ms7.0 Lushan earthquake, 2013. Sci. China Earth Sci. 56 (7), 1187–1192.
Liu, J., Yi, G.X., Zhang, Z.W., Guan, Z.J., Ruan, X., Long, F., Du, F., 2013. Introduction to the Lushan, Sichuan M7.0 earthquake on 20 April 2013. Chin. J. Geophys. 56 (4), 1404–1407 (in Chinese).
Lv, J., Wang, X.S., Su, J.R., Pan, L.S., Li, Z., Yin, L.W., Zeng, X.F., Deng, H., 2013. Hypocentral location and source mechanism of the Ms 7.0 Lushan earthquake sequence. Chin. J. Geophys. 56 (5), 1753–1763 (in Chinese).
Meunier, P., Hovius, N., Haines, A.J., 2008. Topographic site effects and the location of earthquake induced landslides. Earth Planet. Sci. Lett. 275 (3–4), 221–232.
Meunier, P., Uchida, T., Hovius, N., 2013. Landslide patterns reveal the sources of large earthquakes. Earth Planet. Sci. Lett. 363, 27–33.

Moro, M., Saroli, M., Salvi, S., Stramondo, S., Doumaz, F., 2007. The relationship between seismic deformation and deep-seated gravitational movements during the 1997 Umbria–Marche (Central Italy) earthquakes. Geomorphology 89 (3–4), 297–307.
Murphy, W., 1995. The geomorphological controls on seismically triggered landslides during the 1908 Straits of Messina earthquake, Southern Italy. Q. J. Eng. Geol. Hydrogeol. 28 (1), 61–74.
Osmundsen, P.T., Henderson, I., Lauknes, T.R., Larsen, Y., Redfield, T.F., Dehls, J., 2009. Active normal fault control on landscape and rock-slope failure in northern Norway. Geology 37 (2), 135–138.
Owen, L.A., Kamp, U., Khattak, G.A., Harp, E.L., Keefer, D.K., Bauer, M.A., 2008. Landslides triggered by the 8 October 2005 Kashmir earthquake. Geomorphology 94 (1–2), 1–9.
Papathanassiou, G., Valkaniotis, S., Ganas, A., Pavlides, S., 2013. GIS-based statistical analysis of the spatial distribution of earthquake-induced landslides in the island of Lefkada, Ionian Islands, Greece. Landslides 10 (6), 771–783.
Parise, M., 2000. Erosion rates from seismically-induced landslides in Irpinia, southern Italy. Proc. 8th Int. Symposium on Landslides, Cardiff vol. 3, pp. 1159–1164.
Parker, R.N., Densmore, A.L., Rosser, N.J., De Michele, M., Li, Y., Huang, R.Q., Whadcoat, S., Petley, D.N., 2011. Mass wasting triggered by the 2008 Wenchuan earthquake is greater than orogenic growth. Nat. Geosci. 4 (7), 449–452.
Parsons, T., Ji, C., Kirby, E., 2008. Stress changes from the 2008 Wenchuan earthquake and increased hazard in the Sichuan basin. Nature 454 (7203), 509–510.
Pearce, A.J., O'Loughlin, C.L., 1985. Landsliding during a M 7.7 earthquake: Influence of geology and topography. Geology 13 (12), 855–858.
Plafker, G., Ericksen, G.E., Concha, J.F., 1971. Geological aspects of the May 31, 1970, Peru earthquake. Bull. Seismol. Soc. Am. 61 (3), 543–578.
Pourghasemi, H.R., Jirandeh, A., Pradhan, B., Xu, C., Gokceoglu, C., 2013. Landslide susceptibility mapping using support vector machine and GIS at the Golestan Province, Iran. J. Earth Syst. Sci. 122 (2), 349–369.
Prentice, C.S., Schwartz, D.P., 1991. Re-evaluation of 1906 surface faulting, geomorphic expression, and seismic hazard along the San Andreas fault in the southern Santa Cruz Mountains. Bull. Seismol. Soc. Am. 81 (5), 1424–1479.
Qi, S.W., Xu, Q., Lan, H.X., Zhang, B., Liu, J.Y., 2010. Spatial distribution analysis of landslides triggered by 2008.5.12 Wenchuan Earthquake, China. Eng. Geol. 116 (1–2), 95–108.
Richardson, N.J., Densmore, A.L., Seward, D., Fowler, A., Wipf, M., Ellis, M.A., Li, Y., Zhang, Y., 2008. Extraordinary denudation in the Sichuan Basin: Insights from low-temperature thermochronology adjacent to the eastern margin of the Tibetan Plateau. J. Geophys. Res. Solid Earth (1978–2012) 113 (B4) (23 pages).
Rodriguez, C.E., Bommer, J.J., Chandler, R.J., 1999. Earthquake-induced landslides: 1980–1997. Soil Dyn. Earthq. Eng. 18 (5), 325–346.
Royden, L.H., Burchfiel, B.C., King, R.W., Wang, E., Chen, Z.L., Shen, F., Liu, Y.P., 1997. Surface deformation and lower crustal flow in eastern Tibet. Science 276 (5313), 788–790.
Royden, L.H., Burchfiel, B.C., van der Hilst, R.D., 2008. The geological evolution of the Tibetan Plateau. Science 321 (5892), 1054–1058.
Sato, H.P., Sekiguchi, T., Kojiroi, R., Suzuki, Y., Iida, M., 2005. Overlaying landslides distribution on the earthquake source, geological and topographical data: the Mid Niigata prefecture earthquake in 2004, Japan. Landslides 2 (2), 143–152.
Sato, H.P., Hasegawa, H., Fujiwara, S., Tobita, M., Koarai, M., Une, H., Iwahashi, J., 2007. Interpretation of landslide distribution triggered by the 2005 Northern Pakistan earthquake using SPOT 5 imagery. Landslides 4 (2), 113–122.
Sepúlveda, S.A., Serey, A., Lara, M., Pavez, A., Rebolledo, S., 2010. Landslides induced by the April 2007 Aysén Fjord earthquake, Chilean Patagonia. Landslides 7 (4), 483–492.
Shan, B., Xiong, X., Zheng, Y., Jin, B.K., Liu, C.L., Xie, Z.J., Hsu, H.T., 2013. Stress changes on major faults caused by 2013 Lushan earthquake and its relationship with 2008 Wenchuan earthquake. Sci. China Earth Sci. 56 (7), 1169–1176.
Shroder, J.F., Weihs, B.J., 2010. Geomorphology of the Lake Shewa landslide dam, Badakhshan, Afghanistan, using remote sensing data. Geogr. Ann. Ser. A, Phys. Geogr. 92 (4), 469–483.
Stein, R.S., King, G.C.P., 1984. Seismic potential revealed by surface folding: 1983 Coalinga, California, earthquake. Science 224 (4651), 869–872.
Su, F.H., Cui, P., Zhang, J.Q., Gan, G.B., 2013. Rockfall and landslide susceptibility assessment in Lushan earthquake region. J. Mt. Sci. 31 (4), 502–509 (in Chinese).
Tan, X.B., Yuan, R.M., Xu, X.W., Chen, G.H., Klinger, Y., Chang, C.P., Ren, J.J., Xu, C., Li, K., 2012. Complex surface rupturing and related formation mechanisms in the Xiaoyudong area for the 2008 Mw 7.9 Wenchuan Earthquake, China. J. Asian Earth Sci. 58, 132–142.
Tan, X.B., Li, Y.H., Xu, X.W., Chen, W.Y., Xu, C., Yu, G.H., 2013. Cenozoic fault activity of the southern segment of the Longmenshan thrust belt: Evidence from low-temperature thermochronology data. Seismol. Geol. 35 (3), 506–517 (in Chinese).
Tang, C., van Asch, T.W.J., Chang, M., Chen, G.Q., Zhao, X.H., Huang, X.C., 2012. Catastrophic debris flows on 13 August 2010 in the Qingping area, southwestern China: The combined effects of a strong earthquake and subsequent rainstorms. Geomorphology 139–140, 559–576.
Tapponnier, P., Xu, Z.Q., Roger, F., Meyer, B., Arnaud, N., Wittlinger, G., Yang, J.S., 2001. Oblique stepwise rise and growth of the Tibet Plateau. Science 294 (5547), 1671–1677.
Tatard, L., Grasso, J.R., 2013. Controls of earthquake faulting style on near field landslide triggering: The role of coseismic slip. J. Geophys. Res. Solid Earth 118 (6), 2953–2964.
ten Brink, U.S., Geist, E.L., Andrews, B.D., 2006. Size distribution of submarine landslides and its implication to tsunami hazard in Puerto Rico. Geophys. Res. Lett. 33 (11), L11307.
Tibaldi, A., Ferrari, L., Pasquare, G., 1995. Landslides triggered by earthquakes and their relations with faults and mountain slope geometry: an example from Ecuador. Geomorphology 11 (3), 215–226.
Toda, S., Lin, J., Meghraoui, M., Stein, R.S., 2008. 12 May 2008 M = 7.9 Wenchuan, China, earthquake calculated to increase failure stress and seismicity rate on three major fault systems. Geophys. Res. Lett. 35 (L17305) (6 pages).
US Geological Survey, 2013. Shakemap usb000gcdd, USGS ShakeMap: Western Sichuan, China (Instrumental Intensity). Map Version 4 (http://earthquake.usgs.gov/earthquakes/shakemap/global/shake/b000gcdd).
Wang, G.L., 2015. Comparison of the landslides triggered by the 2013 Lushan earthquake with those triggered by the strong 2008 Wenchuan earthquake in areas with high seismic intensities. Bull. Eng. Geol. Environ. 74 (1), 77–89.
Wang, C.-Y., Chang, C.-H., Yen, H.-Y., 2000. An interpretation of the 1999 Chi-Chi earthquake in Taiwan based on the thin-skinned thrust model. Terr. Atmos. Ocean. Sci. 11 (3), 609–630.
Wang, Q., Zhang, P.Z., Freymueller, J.T., Bilham, R., Larson, K.M., Lai, X.A., You, X.Z., Niu, Z.J., Wu, J.C., Li, Y.X., Liu, J.N., Yang, Z.Q., Chen, Q.Z., 2001. Present-day crustal deformation in China constrained by global positioning system measurements. Science 294 (5542), 574–577.
Wang, W.N., Nakamura, H., Tsuchiya, S., Chen, C.C., 2002. Distributions of landslides triggered by the Chi-chi Earthquake in Central Taiwan on September 21, 1999. Landslides 38 (4), 318–326.
Wang, H.B., Sassa, K., Xu, W.Y., 2007. Analysis of a spatial distribution of landslides triggered by the 2004 Chuetsu earthquakes of Niigata Prefecture, Japan. Nat. Hazards 41 (1), 43–60.
Wang, W.M., Hao, J.L., Yao, Z.X., 2013. Preliminary result for rupture process of Apr. 20, 2013, Lushan earthquake, Sichuan, China. Chin. J. Geophys. 56 (4), 1412–1417 (in Chinese).
Wang, M., Yang, W.T., Shi, P.J., Xu, C., Liu, L.Y., 2014. Diagnosis of vegetation recovery in mountainous regions after the Wenchuan Earthquake. IEEE J. Sel. Top. Appl. Earth Obs. Remote Sens. 7 (7), 3029–3037.
Weiss, A.D., 2001. Topographic position and landforms analysis. http://www.jennessent.com/downloads/tpi-poster-tnc_18x22.pdf.
Xie, Z.J., Jin, B.K., Zheng, Y., Ge, C., Xiong, X., Xiong, C., Hsu, H.T., 2013. Source parameters inversion of the 2013 Lushan earthquake by combining teleseismic waveforms and local seismograms. Sci. China Earth Sci. 56 (7), 1177–1186.
Xu, C., 2013a. Assessment of earthquake-triggered landslide susceptibility based on expert knowledge and information value methods: A case study of the 20 April 2013 Lushan, China Mw6.6 earthquake. Disaster Adv. 6 (13), 119–130.
Xu, C., 2013b. Correlations of earthquake-triggered landslides volume and seismogenic fault: A case study of the 12 May 2008 Wenchuan earthquake, China. International Symposium & 9th Asian Regional Conference of IAEG, Global View of Engineering Geology and the Environment. Taylor & Francis Group, London. ISBN: 978-1-138-00078-0, pp. 93–98 (Beijing:).
Xu, C., 2014a. Preparation of earthquake-triggered landslide inventory maps using remote sensing and GIS technologies: Principles and case studies. Geosci. Front. http://dx.doi.org/10.1016/j.gsf.2014.03.004.
Xu, C., 2014b. Do buried-rupture earthquakes trigger less landslides than surface-rupture earthquakes for reverse faults? Geomorphology 216, 53–57.
Xu, C., Xiao, J.Z., 2013. Spatial analysis of landslides triggered by the 2013 Ms 7.0 Lushan earthquake: A case study of a typical rectangle area in the northeast of Taiping town. Seismol. Geol. 35 (2), 436–451 (in Chinese).
Xu, C., Xu, X.W., 2012. Comment on "Spatial distribution analysis of landslides triggered by 2008.5. 12 Wenchuan Earthquake, China" by Shengwen Qi, Qiang Xu, Hengxing Lan, Bing Zhang, Jianyou Liu [Engineering Geology 116 (2010) 95–108]. Eng. Geol. 133–134, 40–42.
Xu, C., Xu, X.W., 2013. Response rate of seismic slope mass movements related with the 2008 Wenchuan Earthquake and its spatial distribution analysis. Chin. J. Rock Mech. Eng. 32 (S2), 3888–3908 (in Chinese).
Xu, C., Xu, X.W., 2014a. Statistical analysis of landslides caused by the Mw 6.9 Yushu, China, earthquake of April 14, 2010. Nat. Hazards 72 (2), 871–893.
Xu, C., Xu, X.W., 2014b. The spatial distribution pattern of landslides triggered by the 20 April 2013 Lushan earthquake of China and its implication to identification of the seismogenic fault. Chin. Sci. Bull. 59 (13), 1416–1424.
Xu, Z.Q., Ji, S.C., Li, H.B., Hou, L.W., Fu, X.F., Cai, Z.H., 2008. Uplift of the Longmen Shan range and the Wenchuan earthquake. Episodes 31 (3), 291–301.
Xu, C., Dai, F.C., Chen, J., Tu, X.B., Xu, L., Li, W.C., Tian, W., Cao, Y.B., Yao, X., 2009a. Identification and analysis of secondary geological hazards triggered by a magnitude 8.0 Wenchuan earthquake. J. Remote Sens. 13 (4), 745–762.
Xu, C., Dai, F.C., Yao, X., 2009b. Incidence number and affected area of Wenchuan earthquake-induced landslides. Sci. Technol. Rev. 27 (11), 79–81 (in Chinese).
Xu, X.W., Wen, X.Z., Yu, G.H., Chen, G.H., Klinger, Y., Hubbard, J., Shaw, J., 2009. Coseismic reverse-and oblique-slip surface faulting generated by the 2008 Mw 7.9 Wenchuan earthquake, China. Geology 37 (6), 515–518.
Xu, C., Dai, F.C., Xu, X.W., 2010. Wenchuan earthquake induced landslides: an overview. Geol. Rev. 56 (6), 860–874 (in Chinese).
Xu, C., Xu, X.W., Dai, F.C., Xiao, J.Z., Tan, X.B., Yuan, R.M., 2012a. Landslide hazard mapping using GIS and weight of evidence model in Qingshui River watershed of 2008 Wenchuan earthquake struck region. J. Earth Sci. 23 (1), 97–120.
Xu, C., Xu, X.W., Dai, F.C., Saraf, A.K., 2012b. Comparison of different models for susceptibility mapping of earthquake triggered landslides related with the 2008 Wenchuan earthquake in China. Comput. Geosci. 46, 317–329.
Xu, C., Dai, F.C., Xu, X.W., Lee, Y.H., 2012c. GIS-based support vector machine modeling of earthquake-triggered landslide susceptibility in the Jianjiang River watershed, China. Geomorphology 145–146, 70–80.
Xu, C., Xu, X.W., Yu, G.H., 2012d. Earthquake triggered landslide hazard mapping and validation related with the 2010 Port-au-Prince, Haiti earthquake. Disaster Adv. 5 (4), 1297–1304.
Xu, C., Xu, X.W., Yao, Q., Wang, Y.Y., 2013a. GIS-based bivariate statistical modelling for earthquake-triggered landslides susceptibility mapping related to the 2008 Wenchuan earthquake, China. Q. J. Eng. Geol. Hydrogeol. 46 (2), 221–236.
Xu, C., Xu, X.W., Dai, F.C., Wu, Z.D., He, H.L., Wu, X.Y., Xu, S.N., Shi, F., 2013b. Application of an incomplete landslide inventory, logistic regression model and its validation for

landslide susceptibility mapping related to the May 12, 2008 Wenchuan earthquake of China. Nat. Hazards 68 (2), 883–900.
Xu, C., Xu, X.W., Zhou, B.G., Yu, G.H., 2013c. Revisions of the M 8.0 Wenchuan earthquake seismic intensity map based on co-seismic landslide abundance. Nat. Hazards 69 (3), 1459–1476.
Xu, C., Xu, X.W., Yu, G.H., 2013d. Landslides triggered by slipping-fault-generated earthquake on a plateau: an example of the 14 April 2010, Ms 7.1, Yushu, China earthquake. Landslides 10 (4), 421–431.
Xu, C., Xu, X.W., Zheng, W.J., Wei, Z.Y., Tan, X.B., Han, Z.J., Li, C.Y., Liang, M.J., Li, Z.Q., Wang, H., Wang, M.M., Ren, J.J., Zhang, S.M., He, Z.T., 2013e. Landslides triggered by the April 20, 2013 Lushan, Sichuan Province Ms 7.0 strong earthquake of China. Seismol. Geol. 35 (3), 641–660 (in Chinese).
Xu, X.W., Wen, X.Z., Han, Z.J., Chen, G.H., Li, C.Y., Zheng, W.J., Zhang, S.M., Ren, Z.K., Xu, C., Tan, X.B., Wei, Z.Y., Wang, M.M., Ren, J.J., He, Z.T., Liang, M.J., 2013a. Lushan Ms 7.0 earthquake: A blind reserve-fault event. Chin. Sci. Bull. 58 (28–29), 3437–3443.
Xu, X.W., Chen, G.H., Yu, G.H., Cheng, J., Tan, X.B., Zhu, A.L., Wen, X.Z., 2013b. Seismogenic structure of Lushan earthquake and its relationship with Wenchuan earthquake. Earth Sci. Front. 20 (3), 11–20.
Xu, C., Xu, X.W., Gorum, T., van Westen, C.J., Fan, X.M., 2014a. Did the 2008 Wenchuan earthquake lead to a net volume loss? Landslide Science for a Safer Geoenvironment. Proceedings of World Landslide Forum 3, 2–6 June 2014, Beijing 3, pp. 191–196
Xu, C., Xu, X.W., Yao, X., Dai, F.C., 2014b. Three (nearly) complete inventories of landslides triggered by the May 12, 2008 Wenchuan Mw 7.9 earthquake of China and their spatial distribution statistical analysis. Landslides 11 (3), 441–461.
Xu, C., Shyu, J.B.H., Xu, X.W., 2014c. Landslides triggered by the 12 January 2010 Port-au-Prince, Haiti, Mw = 7.0 earthquake: visual interpretation, inventory compiling, and spatial distribution statistical analysis. Nat. Hazards Earth Syst. Sci. 14 (7), 1789–1818.
Xu, C., Xu, X.W., Shyu, J.B.H., Zheng, W.J., Min, W., 2014d. Landslides triggered by the 22 July 2013 Minxian-Zhangxian, China, Mw 5.9 earthquake: Inventory compiling and spatial distribution analysis. J. Asian Earth Sci. 92, 125–142.
Xu, C., Xu, X.W., Pourghasemi, H.R., Pradhan, B., Iqbal, J., 2014e. Volume, gravitational potential energy reduction, and regional centroid position change in the wake of landslides triggered by the 14 April 2010 Yushu earthquake of China. Arab. J. Geosci. 7 (6), 2129–2138.
Xu, C., Xu, X.W., Shyu, J.B.H., Gao, M.X., Tan, X.B., Ran, Y.K., Zheng, W.J., 2015. Landslides triggered by the 20 April 2013 Lushan, China, Mw 6.6 earthquake from field investigations and preliminary analyses. Landslides 12 (2), 365–385.
Yagi, H., Sato, G., Higaki, D., Yamamoto, M., Yamasaki, T., 2009. Distribution and characteristics of landslides induced by the Iwate–Miyagi Nairiku Earthquake in 2008 in Tohoku District, Northeast Japan. Landslides 6 (4), 335–344.
Yalcin, A., 2008. GIS-based landslide susceptibility mapping using analytical hierarchy process and bivariate statistics in Ardesen (Turkey): Comparisons of results and confirmations. Catena 72 (1), 1–12.
Yilmaz, I., 2009. Landslide susceptibility mapping using frequency ratio, logistic regression, artificial neural networks and their comparison: A case study from Kat landslides (Tokat—Turkey). Comput. Geosci. 35 (6), 1125–1138.
Yin, Y.P., Wang, F.W., Sun, P., 2009. Landslide hazards triggered by the 2008 Wenchuan earthquake, Sichuan, China. Landslides 6 (2), 139–152.
Yin, Y.P., Li, B., Wang, W.P., 2015. Dynamic analysis of the stabilized Wangjiayan landslide in the Wenchuan Ms 8.0 earthquake and aftershocks. Landslides 12 (3), 537–547.
Yuan, R.M., Deng, Q.H., Cunningham, D., Xu, C., Xu, X.W., Chang, C.P., 2013. Density distribution of landslides triggered by the 2008 Wenchuan earthquake and their relationships to peak ground acceleration. Bull. Seismol. Soc. Am. 103 (4), 2344–2355.
Zeng, X.F., Luo, Y., Han, L.B., Shi, Y.L., 2013. The Lushan Ms 7.0 earthquake on 20 April 2013: a high-angle thrust event. Chin. J. Geophys. 56 (4), 1418–1424 (in Chinese).
Zhang, P.Z., Wen, X.Z., Shen, Z.K., Chen, J.H., 2010. Oblique, high-angle, listric-reverse faulting and associated development of strain: The Wenchuan earthquake of May 12, 2008, Sichuan, China. Annu. Rev. Earth Planet. Sci. 38, 353–382.
Zhang, J.Q., Su, F.H., Fan, J.R., 2013. Distribution of landslides and collapses induced by 2013 "4.20" Lushan earthquake and hazards assessment: a case study of S210 highway. J. Mt. Sci. 31 (5), 616–623.
Zhou, W., Tang, C., 2014. Rainfall thresholds for debris flow initiation in the Wenchuan earthquake-stricken area, southwestern China. Landslides 11 (5), 877–887.
Zhou, Q., Jiang, Y.F., Wu, G., Chen, G.G., 2014. Distribution of coseismic landslides in Lushan earthquake and discussion on related problems. Seismol. Geol. 36 (2), 344–357 (in Chinese).